UNIVERSITÀ
DEGLI STUDI
DI PADOVA

DIPARTIMENTO
DI INGEGNERIA

DIPARTIMENTO DI INGEGNERIA DELL'INFORMAZIONE

CORSO DI LAUREA IN INGEGNERIA BIOMEDICA

Characterization and detection of Detonation Nanodiamonds using Raman spectroscopy, Luminescence spectroscopy and Particle Image Velocimetry

Relatore: Prof. Andrea Bagno

Laureando: Federico Coga

1217343

Correlatori: Ph.D. Dariusz Witkowski, Ph.D. Anna Karczemska

ANNO ACCADEMICO 2021 – 2022

18 / 07 / 2023

Acknowledgments

I would like to sincerely thank Ph.D. Dariusz Witkowski and Ph.D. Anna Karczemska from the Institute of Turbomachinery of Lodz University of Technology (Instytut Maszyn Przepływowych) for the opportunity to work with them. For all the support, patience and help through all the project period, and for the trust you put on me, I'm thankful. It's been a pleasure and an honour to participate in this project.

I also want to thank Ph.D. Prof. Andrea Bagno from the Department of Industrial Engineering of University of Padova, specifically for the trust he gave me on the carrying on this project, always following the development of the thesis from Italy during my mobility period.

My thanks go also to:
Ph.D. Alicja Olejnik, from the Institute of Applied Radiation Chemistry of Lodz University of Technology (Międzyresortowy Instytut Techniki Radiacyjnej), for enabling the creation of our samples of Nanodiamonds in their chemistry laboratory;
Ph.D. Marcin Kozanecki, from the Department of Molecular Physics of Lodz University of Technology (Katedra Fizyki Molekularnej), for the help with the Raman spectroscopy and luminescence study of nanodiamonds in their chemistry laboratory;
to Ph.D Krzysztof Olasek, from the Institute of Turbomachinery of Lodz University of Technology (Instytut Maszyn Przepływowych), for permitting us to use the laboratory and the PIV software for the study.

ABSTRACT

The study focuses its attention on the characterization of two types of Nanodiamonds (RT DND and RT DND LN) that showed the best photoluminescence behaviour as previously studied [38]. For this aim, Raman spectroscopy and photoluminescence spectroscopy are two of the best methods for studying and analysing the luminescence spectra of carbon material including NDs. Raman spectroscopy is a very powerful tool for understanding the behaviour of excited NDs through all the spectra [37]. Photoluminescence spectroscopy will confirm the luminescence properties of the NDs showing the wavelength range where the NDs give the best light response (around 680 nm) and will verify the difference between unmodified (natural purified, RT DND) and modified (nitrogenized, RT DND LN) NDs in the emission of light when excited: the nitrogenized one have a wider broad spectra and a higher emission value thanks to the presence of vacancies and so of colour centers that allows the luminescence phenomena []. After the characterization, the PIV study will be carried on, verifying the eventual presence of a difference between the detection of only water particles (demineralized), of water/RT-DND mixture and water/RT-DND-LN mixture when sprayed from an airbrush end excited by the laser plane at 532 nm. For the three different samples various test were made with three main changing variables: pressure of airbrush, nozzle diameter for the airbrush and the exposure time of the PIV camera. If a difference is observed, there will be the definition of the best configurations of the three variables that allow the best visualization of the NDs particles during their stream path.

Keywords: Nanodiamonds, photoluminescence, spectroscopy, PIV

ABSTRACT

Lo studio si concentra nella caratterizzazione di due tipi di nano-polvere di diamante da detonazione (RT DND e RT DND LN) selezionati per le loro qualità di fotoluminescenza come citato da Z. Novak, A. Karczemska, D. Witkowski [38]. A questo fine, le tecniche di spettroscopia Raman e spettroscopia di fotoluminescenza sono due delle migliori per lo studio di materiali a base di carbonio, compresi i NDs. La spettroscopia di Raman è uno strumento molto potente per comprendere il comportamento dei NDs, quando eccitati, su tutto lo spettro [37]. La spettroscopia di luminescenza conferma le buone proprietà dei NDs mostrando il range di lunghezza d'onda dove la risposta è maggiore (circa 680 nm) e verificando le differenze tra NDs non modificati (naturali purificati, RT DND) e modificati (azotati, RT DND LN) quando eccitati dalla giusta lunghezza d'onda: i NDs azotati mostrano una banda più larga ed un valore di luminescenza più elevato, grazie alla presenza di lacune e quindi dei così chiamati centri di colore che permettono il fenomeno di luminescenza [10]. Conclusa la caratterizzazione lo studio procede, grazie alla tecnologia di Particle Image Velocimetry (PIV), alla verifica di una eventuale differenza nel rilevamento di solo molecole d'acqua (demineralizzata), del campione di acqua/RT DND e del campione acqua/RT DND LN quando erogati da un aerografo ed eccitati da un laser a lunghezza d'onda di 532 nm. Per i tre campioni sono stati eseguiti diversi test variando tre parametri principali: pressione dell'aerografo, diametro dell'ugello dell'aerografo e il tempo di esposizione della fotocamera utilizzata nel PIV. Se notata differenza nei numerosi test, verrà definita la miglior configurazione dei tre parametri che permetta una visualizzazione ottimale delle particelle di NDs come del loro flusso dopo l'erogazione.

Parole chiave: Diamante da detonazione, spettroscopia di fotoluminescenza, PIV

Summary

1) INTRODUCTION

In recent years, carbon and carbon-based nanomaterials have received increasing attention for applications in life sciences. Nanodiamond (ND) stands out as a unique new substance in these applications because it holds several momentous properties such as good biocompatibility, excellent photostability and easy surface functionalizability. Several experiments have shown that NDs has the highest biocompatibility of all carbon-based nanomaterials including carbon blacks, multi-walled nanotubes, single-walled nanotubes and fullerenes. Additionally, the surface of ND can be readily derivatized with various functional groups for either covalent or noncovalent conjugation with biomolecules. Furthermore, some radiation-damaged NDs can emit strong and stable photoluminescence (red or green) from nitrogen-vacancy defect centers embedded in the crystal lattice. These properties together make ND a highly promising nanomaterial for both in vitro and in vivo applications [36]. Carbon-based nanomaterials as NDs have found several applications in many different fields such as bioimaging, biosensing, drug delivery, heat therapy, cells detection.

Particle Image Velocimetry (PIV) is a powerful tool for velocity study and velocity distribution study. These types of flows are nowadays investigated by PIV because of its ability to visualize and quantify the instantaneous velocity field within an entire plane of the flow domain. However, the full understanding of complex flows often requires the use of three-dimensional (3D) measurement methods. The use of planar PIV techniques for study of vortex dynamics in complex flows remains impaired by the two-dimensional approach to phenomenon that occurs in a space with a higher dimensions. the interpretation of such experiments to infer the underlying dynamical system requires a deal of assumptions, a-priori knowledge and sometimes biased by prejudice [15]. In this study PIV will be used for determination of the possibility to detect NDs particles using 532 nm laser and defining parameters that change this functionality (nozzle dimension, airbrush air pressure, camera exposure time).

This study presents a process of characterization and utilization of NDs in PIV system for the possible future purposes of the latter.

2) CARBON

2.1 Allotropic form

Carbon exists in different allotropic forms (diamond, graphite, fullerene, graphene, carbine), some of them can be used in the biomedical field due to their biocompatibility. Therefore, carbon has been applied to coat medical implants, and to produce implantable devices for example for cardiovascular surgery, orthopaedic surgery or dentistry.

Some carbon-based biomaterials are characterized by the following properties:

- good biological tolerance;
- resistance to radiation, both ionizing and non-ionizing;
- blood compatibility;
- athrombogenity;
- specific physicochemical properties that change with the structure.

Nanocrystalline diamonds (NCDs) appear particularly interesting due to their potential applications in industry and bio-medicine, taking into account all their characteristics including biocompatibility. Some of the principal carbon allotropic forms (diamond, graphite, fullerene, carbine) will be presented in the following sections.

2.2 Diamond

In its crystalline unit cell (Figure 1), diamond contains 8 carbon atoms, each one characterized by a tetrahedral coordination [1]. The coordination of each carbon atom reflects the spatial orientation of its sp3 hybridized orbitals. Atomic bonds are directed from a central atom towards the vertexes of the tetrahedron, forming with each other equal angles of 109.5°. The distance between carbon atoms in the crystallographic direction (1-0-0) is 0.154 nm.

Diamond is insoluble in water. It does not conduct electricity. In diamond, each atom is bonded to its neighbours by four strong covalent bonds, leaving no free electrons or ions. Diamond structure can be regarded as a face centered cubic (FCC) lattice of the A1 type, in which carbon atoms occupy fifty percent of tetrahedral interstices. When the (1-1-1) direction of diamond crystalline structure is positioned vertically (Figure 2), folded hexagonal rings with centers of carbon atoms placed in their vertexes are seen in the (1-1-1) plane, situated horizontally. The space filling factor in the diamond structure is low and it amounts to 34%.

The main properties of diamond are summarised in following Table 1 and Table 2 .

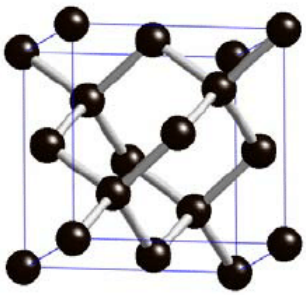

Figure 1: Diamond crystalline unit cell [1]

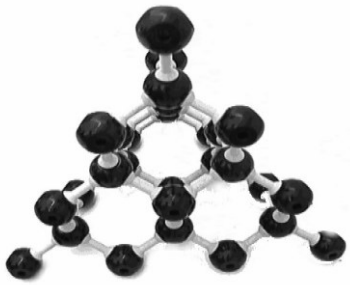

Figure 2: Model of diamond crystalline lattice with a view of the (111) plane [1]

Property	Value	Unit
Hardness	10000	$kg\,mm^{-2}$
Strength, tensile	>1.2	GPa
Strength, compressive	>110	GPa
Density	3.52	$g\,cm^{-3}$
Young's modulus	1220	GPa
Thermal expansion coefficient	0.0000011	K^{-1}
Thermal conductivity	20.0	$W\,cm^{-1}\,K^{-1}$
Debye temperature	2200	K
Optical index of refraction (at 591 nm)	2.41	Dimensionless
Bandgap	5.45	eV

Table 1: Physical properties of diamond [9]

Classification of diamonds.

Type	Feature	Color	Note
Ia	Nitrogen atom concentration up to 0.3%, aggregated nitrogen	Colorless	Most natural diamonds
Ib	Nitrogen atom concentration up to 500 ppm, singly substitutional nitrogen	Yellow, orange	Rare in nature, almost all HPHT diamonds
IIa	No or few nitrogen atoms	Colorless	Rare in nature, the "purest" diamonds
IIb	No or little nitrogen, boron-doped	Blue, gray	Extremely rare in nature, p-type semiconductor

Table 2: Specific features of different types of diamonds [9]

2.3 Graphite

Graphite (Figure 3) allotropic form of carbon is stable under normal pressure and temperature conditions [9]. Graphite has a typical laminar structure (stacked structure of graphene). Atoms are placed in layers, forming hexagons in the (001) plane, with the interlayer distance of 0.142 nm. In one layer, each carbon atom has three closest neighbours. The coordination figure is an equilateral triangle. The space filling factor equals 16.9%, with the assumption that only covalent bonds are present in the structure.

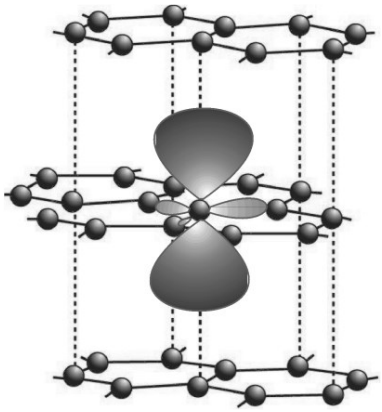

Figure 3: Graphite crystalline unit cell with the electronic structure (three planar sp2 orbitals in (001) plane and one p orbital of one of the atoms marked) [1]

Strong covalent bonds formed of hybridized electronic orbitals sp2, connect carbon atoms in (0-0-1) planes. The fourth electron of each atom is in a state of resonance between three adjacent atoms, forming a weak transitional π bond with the atoms of adjacent layers. The bonds within the (0-0-1) plane are much stronger than the bonds between (0-0-1) planes and, as indicated by interatomic distances, they are also stronger than diamond bonds.

As a result of substantial differences in carbon-carbon bond strength between atoms in one layer and atoms of adjacent layers, graphite is characterized by a strong anisotropy of its physical properties (cleavage, thermal expansion, electrical conductivity, thermal conductivity).

2.4 Fullerenes and nanotubes (graphene derived materials)

Fullerenes (or bulkyballs) are composed exclusively of carbon of varying size and molecules that resembles a hollow sphere or tube (Figure 4) [1]. Fullerenes have been studied comprehensively as related to carbon nanotubes, and have opened a new scientific and technologic field on nano-scale materials since before the advent of graphene in 2004 [2]. Fullerenes constitute an entirely new class of materials, exhibiting properties, relatively easy to determine and to design. They possess exceptional stability as well as advantageous electrical and magnetic properties, which draw significant scientific attention to these compounds, in particular in the context of high capacity battery design and semiconductor technology.

As the word ‘nanotube’ entails in the name of all sorts of carbon nanotubes, the materials consist of only two coaxial cylinders (Figure 5) [2]. The multi-walled sort of nanotubes has an outer diameter as small as 55 Å and an inner diameter as small as 23 Å. In a simple term, carbon nanotubes possess a thickness or diameter approximately of only some

nanometers and the thickness is comparatively about 50,000 times smaller than the width of a human hair and can be up to many centimetres in length. Structurally, a nanotube is cylindrical in shape with one of its ends usually wrapped into a hemisphere of buckyball spherical structure.

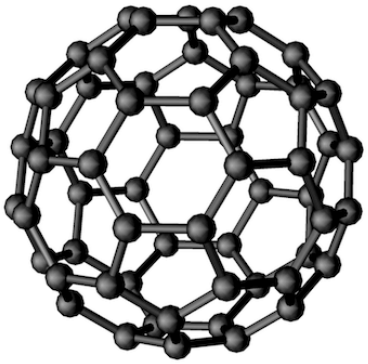

Figure 4: A model of fullerene C60 molecule [5]

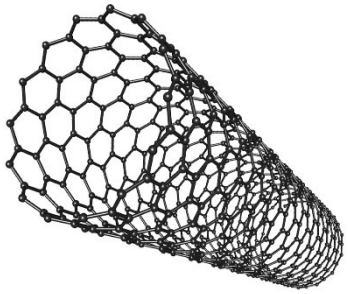

Figure 5: Structure of fullerene nanotube [6]

2.5 Carbine

Carbine constitutes carbon most recently studied allotropic form.

Today, a few forms of carbine are known, among which the most important and the best understood are:

- α-carbine, which contains acetylene bonding (-C=C-), and this is why it can be described as polyacetylene; it has a hexagonal unit cell, z=144, a_o=0.892 nm, c_o=1.536 nm, density $\rho = 2.68 \times 10^3$ kg m^{-3}
- ß-carbine, which contains cumulene bonding (=C=C=), and this is why it can be described as polycumulene; it has a hexagonal unit cell, z=72, a_o=0.824 nm, c_o=0.768 nm, density $\rho = 3.13 \times 10^3$ kg m^{-3} [1].

3) NANODIAMONDS (NDS)

In recent years, nanodiamonds (NDs) have been finding numerous applications in bioengineering and biomedical technology, thanks to their principal characteristics as a nanomaterial, merged with the unique features of carbon in diamond form. In the following sections, nanomaterials properties and characterization will be illustrated, then focusing later on NDs.

3.1 Nanomaterials basic properties

Although nanomaterials themselves are covered by the definition of substance within the REACH legislation (Regulation (EC) No 1907/2006 European Commission 2006), currently the definition of what "nano" means is still under debate [3]. Various organizations proposed some definitions using an upper limit of about 100 nm. It should be noted that most currently used definitions use the size of the primary particle/structure as a starting point. However, when a nanomaterial is in a particulate form, the particles may be present either as single ones or as agglomerates or aggregates. Depending on the nanomaterial, there agglomerates form the majority of the particles. This may lead to the misinterpretation that aggregates of nanoparticles that have external dimensions well beyond 100 nm are not considered nanomaterials. Yet, they retain specific physicochemical properties typical of nanomaterials, most likely due to their large specific surface area (SSA). The uncertainty regarding the presence of nanomaterials (either determined by size, <100 nm, or SSA >60 m^2/g when calculated for <100 nm unit density spheres) in products becomes of major importance when the only information about it relies solely on the information provided by the manufacturer.

Nanomaterials can exist as nano-powders [3], suspended in air (ultrafine particles, nanoparticles, aerosols), or liquid (colloids) and incorporated in solids. For the biological safety evaluation, manufactured nanomaterials need to be dispersed in an appropriate media. The interaction between these media and the nanomaterials can have a profound influence on the behaviour of the suspension. Since dissolution kinetics is frequently proportional to the surface area, nanomaterials are likely to dissolve much more rapidly than larger sized materials.

The properties of matter at the nanoscale level are substantially distinct compared to bulk counterparts. Size-dependent effects become more prominent at the nanoscale. The properties can be obtained tuning the nanomaterial size.

At the nanoscale, electronic properties are substantially different in comparison with bulk materials [4]. For example, boron in bulk form is not considered a metal, whereas a two-dimensional network of boron (borophene) appears to be an excellent 2D metal. Compared to their bulk counterparts, the mechanical properties of nanomaterials are considerably improved due to the increase in crystal perfection and reduction in crystallographic defects.

Electronic properties of semiconductors in the 1–10 nm range are controlled by quantum mechanical considerations [4]. Thus, nanospheres with diameters in the range of 1–10 nm are known as quantum dots. The optical properties of nanomaterials such as quantum dots strongly depend upon their shape and size. A photogenerated electron–hole pair has an exciton diameter on the scale of 1–10 nm. Thus, the absorption and emission of light by semiconductors could be controlled tuning the nanoparticle size in this range. However, in the case of metals, the mean free path of electrons is ∼10–100 nm and, therefore, electronic and optical effects are expected to be observed in the range of ∼10–100 nm.

3.2 Nanomaterials structures

Several classes of nanostructures have been reported in literature (e.g., nanotubes, nanofibres, nanorods) [7], and each single one has specific properties suitable for a clear purpose:

- Nanosphere: nanosphere innovation spins around the use of polymeric, inorganic or their combinational materials, to produce spherical particles with average diameters in nanometric scale. Their nanoscale size and capacity to encapsulate and release drug or active molecules, make them perfect vehicles for these purposes.
- Nanorods: nanorods are NPs that possess dimensions below 100 nm, while the areas of two of the faces have an aspect ratio between 3 and 5. General properties of nanorods are significantly improved when compared to spherical particles. This is because the expansion of the aspect ratio prompts the expansion of excitation of surface plasmons in the NPs. Flexible medication delivery devices using nanoporous layers that comprise gold nanorods and dendrimers, have been shown to give light-activated, on-request pulsatile discharge resources containing exceptionally enhanced therapeutics for an effective patient's recovery.

- Nanostar: different metallic star-shaped nanostructures have been prepared for several biomedical applications. In this case, the strategy requires the production of a gold nanoparticle star (GNS) without the use of lethal surfactants generally required for GNS fabrication, which enhances the biocompatibility of the GNS. A GNS contains various sharp edges, which act like lightning poles to drastically enhance the nearby electromagnetic field.
- Nano Core–Shells: core–shell nanomaterials and nanostructures have turned into an essential research subject in the last couple of decades because of their potential applications in different fields, especially in the delivery of bioactive molecules, etc. Core–shell nanocomposites and nanostructures might possess various sizes and distinctive states of core and shell thickness, with different surface morphologies.
- Nanotubes: among nanotubes, carbon nanotubes, which were invented in 1991, are the most well-known. They are cylindrical structures like a sheet of graphite folded into a chamber topped at one or both ends, finished by a buck ball. Due to their structures, nanotubes can be classified into two types: single-walled carbon nanotubes (SWCNTs) and multiwalled carbon nanotubes (MWCNTs).
- Quantum dots: for both biomedical and modern applications (e.g. Selective nanosensors, Fluorescence applications, capping agents), quantum dots (QDs) are among the most developed entities of NPs widely used in the last decade. The idea of QDs was created in strong glass crystals and a fluid state. According to quantum mechanics, QDs can be defined as any materials that possess higher electrical and optical properties in their nanoscale (2–10 nm) compared to their largescale, which makes them highly recommended for semiconductor applications.
- Nanocrystal and Nanocube Structures: changing metallic or bimetallic (BM) NPs, which start with one shape and then change onto another desired shape, is of significance to nanoscience and nanotechnology. This is because new morphologies of NPs lead to improvement of their exploitable properties. Recently, colloidal inorganic nanocrystals (NCs) have received extensive consideration in a few fields according to their fascinating size-subordinate properties, for example, their quantum control effect and restricted surface plasmonic effect, which are not recognised in their bulk status.

3.2 Diamonds - Type of Nanodiamonds

Thanks to the unique properties of the various structures that it can take, diamond has been part of studies involving carbon nano-structures, called "Nanodiamonds". Numerous methods of production of nanodiamond (ND) particles have been proposed, including the detonation technique, laser ablation, high-energy ball milling of diamond microcrystals grown at high static pressure and high-temperature (HPHT), etc. (Figure 6).

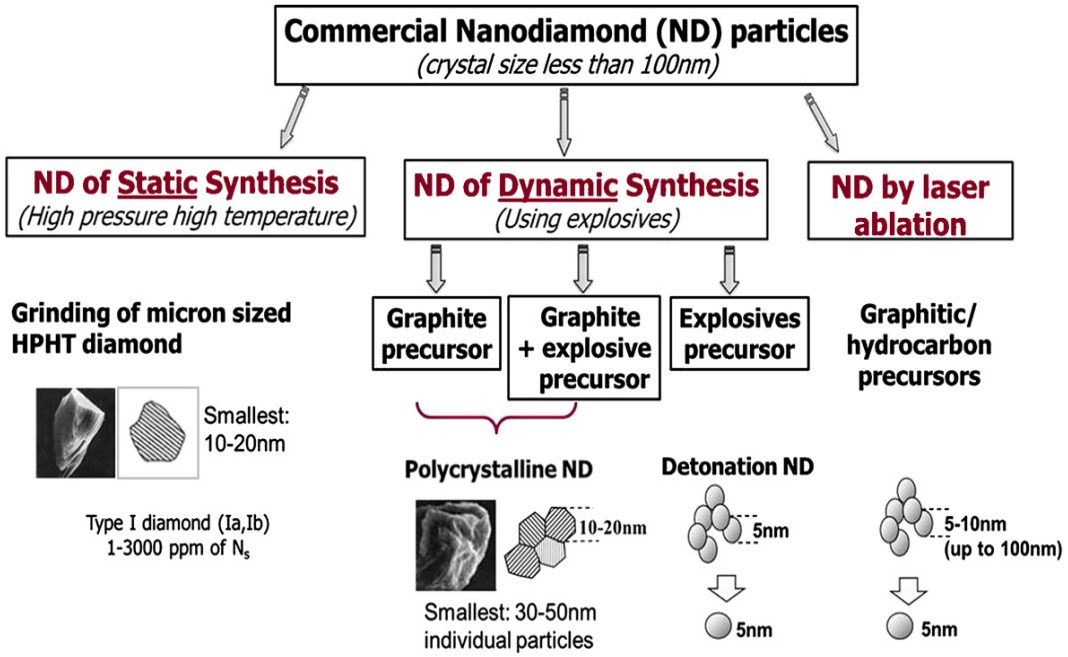

Figure 6: Summary of types of commercial nanodiamonds [8]

Among all these kinds of NDs, the most widely used are those obtained by detonation synthesis (DNDs), produced by detonation of carbon-containing explosives, and HPHT nanodiamond particles, obtained by milling of micron-size HPHT particles [8].

The major differences between DND and HPHT ND are the size of primary particles (monocrystallites) and the state and content of nitrogen impurities in the core of the particles. Moreover, due to the difference in the synthesis (bottom up vs top down approaches), the DND and HPHT NDs have distinct morphological differences. DNDs are advantageous due to the small size of the primary particles produced (4–5 nm) immediately at the synthesis stage, and the established industrial scale production of ton quantities annually.

As-produced DNDs form tight, inseparable aggregates of primary particles. Usually, deaggregation of the aggregates is made by sonication. However, due to recent

advances in DND deaggregation by milling colloidal solutions of primary ND particles 4–5 nm in diameter with spherical morphologies have become readily available.

One of the typical characteristics of HPHT NDs is both presence and structure of nitrogen impurities. HPHT NDs of type Ib have nitrogen impurities primarily in the substitutional state (Ns) at the 100–200 ppm level.

High-energy irradiation of type Ib NDs to form vacancies followed by annealing causes the formation of nitrogen-vacancy (NV) color centers with red emission, while type Ia NDs exhibit green luminescence originating from formation of NVN (H3) centers after irradiation and annealing. NDs synthesized from explosives have not been the preferred candidates for imaging applications based on NV centers since the high N content (up to 2–3 wt%) exists primarily as aggregates of N which render DNDs optically inactive even with irradiation and annealing.

For HPHT NDs, a central focus of many research groups remains the controlled production of nitrogen-vacancy centers in nanoscale diamond for applications as fluorescent biomarkers with high photostability, magnetic sensors with nanoscale resolution, or as efficient single photon emitters for quantum information processing. The synthesis of NDs of a few nanometers in size with specific color centers remains an important goal, and perhaps new methods of nanodiamond particle synthesis are needed to address it.

Additionally, the synthesis of boron-doped nanodiamonds, which are conductive and can be used in electroanalysis, electrochemical double-layer capacitors, and batteries, is an important goal.

3.3 Photoluminescence of NDs

Nanodiamonds can glow, support, and are safe to use [10]. These unique features have made nanodiamonds a superior material for a fast-growing list of applications at present time and in the coming future [10].

First comes an optical property that puts some color on diamond. It is only fitting to start with color centers in diamond. Color centers are crystal defects that absorb light in a spectral region where the crystal itself has no absorption. The term “color center” is derived from the German word Farbenzentren, which was first discovered in alkali halide crystals by Pohl and coworkers in the 1930s [11]. It has later been confirmed both experimentally and theoretically that the Farbenzentren (or F-center) is a crystalline vacancy with captured unpaired electron(s) that absorbs light in the visible region, thus giving various colors to the crystals.

A pure diamond is optically transparent with its transmittance extending from 225 to 2000 nm. The diamond crystal shows only infrared (IR) absorption bands at 2–7 μm resulting from two- and three-phonon excitation processes. The absence of one-phonon absorption is due to the high symmetry of diamond's crystal structure, of which C–C vibrations are IR-inactive.

The major impurity in diamond is nitrogen. Nitrogen concentration in diamonds is typically measured by inert gas fusion analysis, which involves fusing the sample material in a graphite crucible at high temperatures and then determining the amount of the nitrogen gas released by a mass spectrometer. Being uantitative, this method is destructive. IR absorption spectroscopy method, on the other hand, is non-destructive and it has been applied as a tool to characterize nitrogen concentrations.

Increasing nitrogen content to more than 600 ppm could be achieved by doping the solvent catalyst with inorganic nitrogen-containing substances in high concentrations.

Crystal defects are the second source responsible for diamond color. In 1896, French scientist Henri Becquerel accidentally discovered radioactivity while performing phosphorescence experiments with uranium salts. In 1904, in a paper presented to the Royal Society of London, the English scientist William Crookes reported that the exposure of diamonds to radiation generated by radium bromide for several months could give the gem a bluish green to green color [12]. Radium bromide used by Crookes contains radium, which is a highly radioactive element.

It is now known that all isotopes of radium are radioactive and the most stable isotope is Ra-226 with a half-lifetime of 1600 years. The isotope slowly decays to radon, which is a stable inert gas, emitting alpha particles along with the process. Research studies by physicists between 1910 and 1940 had concluded that the color change of diamond was mainly due to the alpha radiation from radium. The color appeared to be confined to a shallow layer on the diamond's surface.

More studies of the effect found that the green or blue-green color could be changed further to various shades of color ranging from yellow to brown by thermal annealing. It was this permanent color enhancement through irradiation combined with high-pressure high-temperature annealing that opened the modern era of diamond treatment.

Systematic investigations of radiation damage in natural and synthetic diamonds were first carried out in the 1950s. Nearly all radiation-damaged diamonds show an absorption

band associated with the neutral vacancy defect (Figure 7a for the molecular structure), designated as V0, in their ultraviolet-visible (UV-Vis) spectra. The neutral vacancy, known as the GR1 center where GR stands for "general radiation", is one of the best characterized optical defects in diamond [8]. When exposed to orange-red light, the center emits near-infrared photoluminescence at approximately 800 nm (Figure 7) with a quantum yield of only 1.4% at low temperature. Although GR1 is not a good chromophore for fluorescence imaging because of such a low quantum yield, it can be produced with a high number density (>100 ppm) by extensive irradiation without the need of thermal annealing.

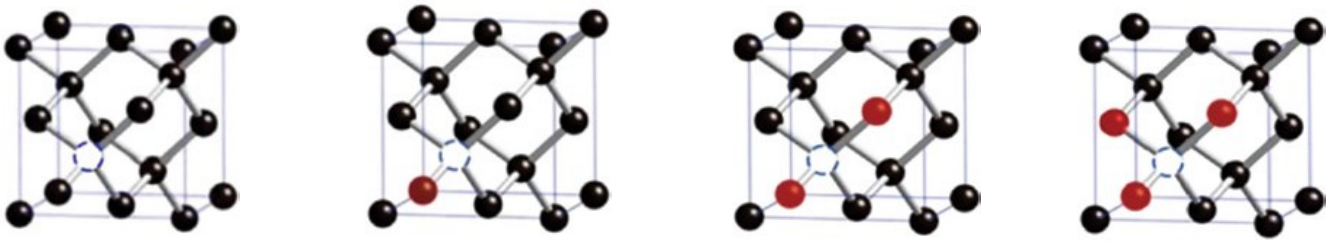

Figure 7: Structures of vacancy-related colour centers in diamond: (a) V0, (b) NV, (c) H3, and (d) N3. The carbon atoms, nitrogen atoms, and vacancies are denoted by black spheres, dark red spheres, and blue dashed circles, respectively [10]

In type Ia diamonds, the ND1 center has a peak intensity comparable to that of GR1 but can barely be detectable in type IIa diamonds (Figure 8 a and b). There is no distinct photoluminescence band associated with ND1. It has been reported that intense UV illumination of the ND1 band results in a reduction of its absorption strength but concurrently increases the GR1 band intensity, presumably due to the release of the trapped electrons from the vacancies.

Vacancies in diamond once produced by radiation damage are static at room temperature. They start to migrate when the irradiated diamond is heated above 500 °C. The activation energy barrier is 2.3 eV (or 53 kcal mol−1). For type Ib diamond containing atomic nitrogen, while some of the vacancies are annihilated at the surface, the majority of them can form stable complexes (i.e. the nitrogen-vacancy (NV) centers) with nitrogen atoms in the diamond matrix.

The NV center in diamond is a point defect comprising a substitutional nitrogen atom adjacent to a vacancy in a C3v point group symmetry (Figure 7b). Similar to the vacancies GR1 and ND1, a NV center can exist in one of the two states: NV0 or NV−. The corresponding emission bands peak approximately at 600 and 700 nm for NV0 and NV−,

respectively (Figure 9), with the associated lifetimes of 11.6 ns and 19 ns. Compared to NV−, NV0 is significantly lower in concentration due to the transfer of electrons from N0 to NV0 during annealing.

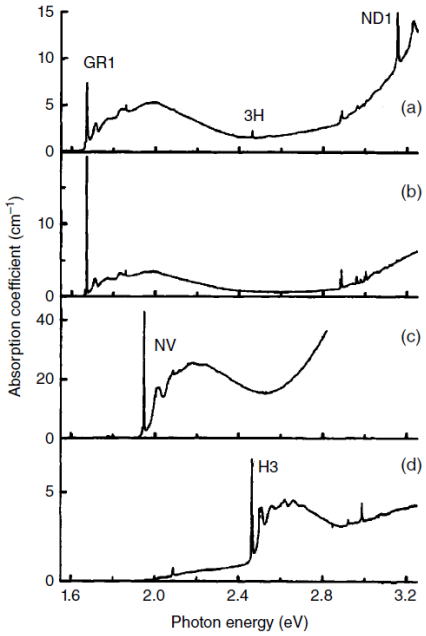

Figure 8: UV-Vis absorption spectra of natural and synthetic diamonds after irradiation at room temperature with 2-MeV electrons: (a) type Ia, (b) type IIa, (c) type Ib with additional annealing, and (d) type Ia with additional annealing. All the spectra were recorded at liquid-nitrogen temperature [10].

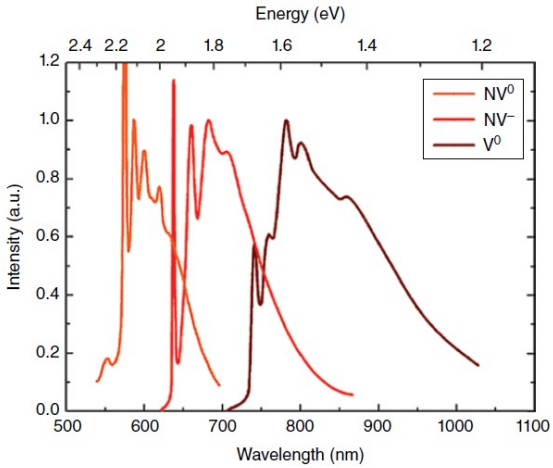

Figure 9: Luminescence spectra of NV0, NV–, and V0 in diamond at 77 K. The characteristic ZPLs are located at 575, 637, and 741 nm, respectively [10].

For the NV centers in diamond, the relative concentrations of the two different forms, NV0 and NV−, may be changed by a shift of the Fermi level due to neutron irradiation or laser illumination. Figure 10 presents a schematic energy diagram of the photoinduced ionization and recombination of NV− and NV0 with respect to the energy band gap (Eg = 5.5 eV) of diamond.

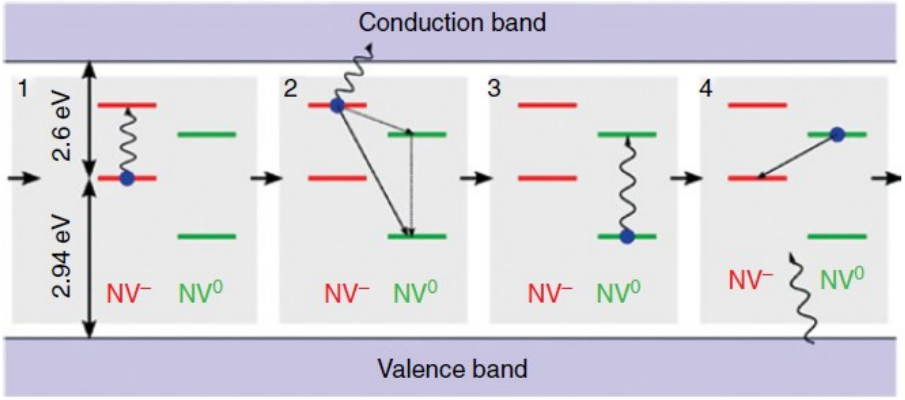

Figure 10: Schematic illustration of the photoinduced ionization and recombination of NV−and NV0. Processes 1 and 2 are associated with ionization and processes 3 and 4 are associated with recombination. [10].

For the charge recombination processes (3 and 4 in Figure 10), the NV0 center is first photoexcited, followed by energy transfer and capture of an electron from the valence band to form NV−. At the steady state, the NV− population is close to 75% under continuous laser excitation in the 450–610 nm wavelength range.

3.3.1 Colour centers

Over the past six decades optical properties of vacancy-related color centers in natural and synthetic diamonds have been extensively studied using various spectroscopic techniques. Table 3 summarizes the spectroscopic properties of V0, V−, NV0, NV−, H3, N3, and SiV− centers in bulk diamonds. Of these seven color centers, H3, N3 and NV− deserves special attention with an in-depth discussion for its remarkable optical and magnetic properties.

Center	Point group	ZPL (nm)	τ (ns)	QE (%)
V^0 (GR1)	T_d	741	2.55	1.4
V^- (ND1)	T_d	394	—	—
NV^-	C_{3v}	637	11.6	99
NV^0	C_{3v}	575	19	—
N–V–N (H3)	C_{2v}	503	16	95
N_3+V (N3)	C_{3v}	415	41	29
SiV^-	D_{3d}	738	1.28	—

Table 3: Spectroscopic properties of vacancy - related colour centers in bulk diamonds [10]

3.3.2 H3 and N3

The smallest ND aggregate, known as the A center, consists of two adjacent lattice points occupied by two nitrogen atoms. They can combine with vacancies to form a stable nitrogen–vacancy complex, designated as H3 or N–V–N, with a C2v point group symmetry (Figure 7c) For diamonds containing high-density ensembles of H3 centers, bright green emission emerges when they are exposed to blue light around 470 nm. Taking advantage of these remarkable photophysical properties, together with the high thermal conductivity and the non-hygroscopic characteristic of the material, Rand and coworkers explored the possibility of using type Ia diamonds containing H3 as a high-stability lasing medium for room-temperature color center lasers [10]. N3 is another color center frequently discovered in natural diamonds after irradiation and annealing treatments. Often produced alongside H3, this structural defect consists of three substitutional nitrogen atoms surrounding a vacancy, designated as N3 + V, in a point group symmetry of C3v (Figure 7d). The blue emission of this center is most commonly observed in natural diamonds when exposed to UV photons (wavelength < 225 nm), which excite electrons from the valence band to the conduction band.

3.3.3 NV-

The NV− center consists of three carbons and one nitrogen surrounding an anionic vacancy in a tetrahedral configuration that belongs to a C3v point group symmetry [10]. It is a six-electron system: 1 e^- from each of the three carbons, 2 e^- from N, and 1 e^- of the vacancy. Linear combinations of atomic orbitals (LCAO) suggest a ground electronic configuration of a1 2a1 2e2. In the optical region, the NV− center shows a characteristic ZPL in both absorption and emission spectra at 637 nm.

Further studies found that the photoluminescence of the transition had a lifetime of 11.6 ns for a synthetic type Ib diamond with a quantum yield close to 1. Moreover, the fluorescence intensity was exceptionally stable as the center acted like a pseudo-atom in an inert and highly thermally conductive matrix. The high photostability allows facile detection of individual NV− centers by fluorescence imaging, especially in biological systems. At present, the NV− in diamond is the only known solid state system that allows detection and manipulation of the spin states of a single localized electron at room temperature. In addition, the NV− center has an exceptionally long coherence time and as such its spin states have been reported to remain coherent for longer than 1 ms in

isotope-free bulk diamonds. All these features combined together make diamonds hosting NV− centers an extraordinary tool for ultra-sensitive measurements of temperature, magnetic field, electric field, and mechanical stress at the nanometer scale.

The NV− center is particularly appealing for use in biological imaging and tracking applications owing to its unmatchable physicochemical properties as summarized below [10]:

- NV− centers can be produced as high-density ensembles in nanoscale diamonds, which are biologically inert and photostable materials.
- Emission band of NV− peaks at 685 nm where the light has a long penetration depth through tissue, and more than 70% of the emitted photons lie in the near infrared window of bioimaging.
- Fluorescence lifetime of NV− is significantly longer than those of cell and tissue autofluorescence, allowing for time-gated fluorescence imaging both in vitro and in vivo.
- Fluorescence intensity of NV− can be modulated by applying either sinusoidal magnetic field or sinusoidal microwave radiation to achieve background-free detection in tissue imaging.

The combination of these outstanding features has attracted scientists to employ FNDs containing high-density ensembles of the NV− centers as bioimaging contrast agents.

3.4 Applications of NDs

Nanodiamonds (NDs) have excellent mechanical and optical properties, large surface area, easy bioconjugation and high biocompatibility, which makes them suitable for various applications (Figure 11) [13]. In recent years, NDs have received considerable attention in nanomedicine, and some noteworthy progress has been achieved. In the following section, we focus on the applications of NDs in nanomedicine, including bioimaging, drug delivery, and biosensing [13].

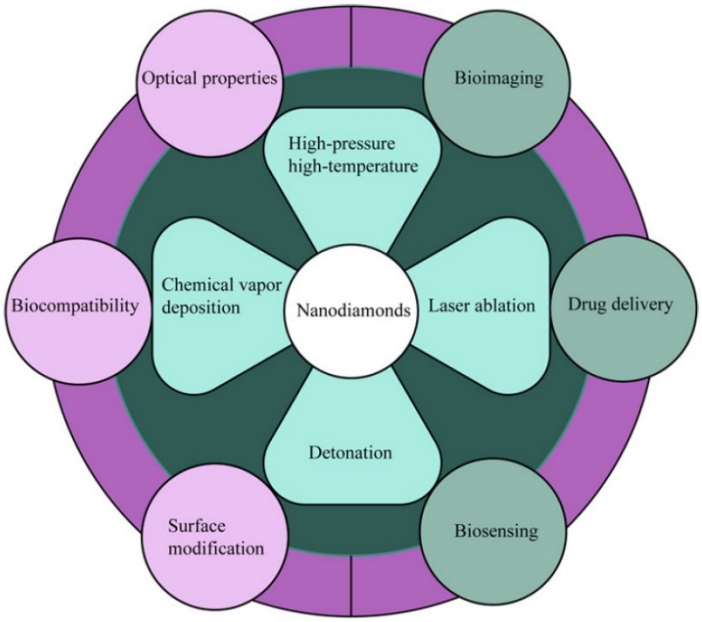

Figure 11: NDs properties and applications [11]

3.4.1 Bioimaging

Bioimaging is a very interesting research topic, which can monitor the metabolic process and disease-related changes of the body through non-invasive insight into the tissues and cells of living organisms [13]. Compared to other nanomaterials as contrast agents, NDs have recently emerged as a promising candidate. Its small size, stable fluorescence and high biocompatibility of NDs make them suitable for bioimaging applications. In particular, NV center of fluorescent NDs is an atom-like light-emitting source and its electron spins can be optically detected and modulated even at room temperature. In addition, most of its emission lies in the near-infrared range, which can be greatly useful for a high-resolution imaging and diagnosis in biomedicine. Although NDs are widely used in cell imaging due to their excellent fluorescence, they possess remarkable penetration limits in histological applications. Magnetic resonance imaging (MRI) is a type of tomography that uses magnetic resonance to extract electromagnetic signals from the body and reconstruct information about the body. It has played an irreplaceable role in clinical diagnosis. In recent years, many advances have been made in the application of NDs in MRI.

3.4.2 Drug delivery

Whether a nanomaterial is suitable for drug delivery depends on its biocompatibility, dispersibility in water, ability to carry drugs and potential of targeted therapy [13]. NDs can be modified with specific functional groups by surface treatment. Thus, drugs can be physically or chemically linked to NDs for delivery. *Zhang et al* reported on an inclusive multicomponent NDs-based drug delivery system with simultaneous capabilities in targeting, imaging and enhanced therapy [22]. *Roy et al*. delivered NDs based anti-HIV drugs to the brain [23]. Our group prepared nanocomposites that enable drugs to be delivered in cells by connecting NDs with up-conversion NaYF4: Yb, Er nanoparticles (UCNPs). UCNPs can absorb the near-infrared light and convert it into higher energy photons in a very wide range from ultraviolet to near-infrared light. The composite material also shows high drug storage and release characteristics, and can be used as a promising anti-cancer drug carrier targeting tumor sites [23]. NDs can be combined together with other nanoparticles to form multifunctional platforms. By coordinating two different rare-earth ions at the same time, the nano-platform is fluorescent and paramagnetic, and can detect mice and cancer cells in vitro and in vivo, respectively [13]. In addition, the nano-platform has a good drug loading capacity. Through the reasonable modification of NDs, it can be used in the fields of targeted drug transportation, cancer treatment, protein separation and purification, etc. This serves as a promising foundation for continued NDs development and potential clinical application.

3.4.3 Biosensing

A biosensor generally refers to an analysis device that converts biological reactions into electrical signals [13]. Biosensor is a new and high-tech tool, which has been developed for supplications in the following fields: biology, chemistry, physics, medicine and electronics. Since the discovery of NDs, many achievements have been made in various fields. Similarly, NDs have also made some progress in the field of biosensors. *Zhao et al*. reported the use of NDs modified gold electrodes for glucose biosensing. Glucose oxidase modified NDs were attached to the surface of gold electrodes [21]. NDs pre-modified the anode of the electrode, which not only increased the electron transfer rate in the NDs chip, but also significantly improved the reduction of dissolved oxygen. The negative potential of glucose can be detected by monitoring the current change of oxygen reduction. The glucose sensor can selectively perform electrochemical analysis of glucose in the presence of common interference substances, such as ascorbic acid, acetaminophen and uric acid.

3.4.4 Heat therapy

Heat therapy is a method of killing tumor cells by heating the lesion site according to the different sensitivity of tumor cells and normal cells to heat [13]. Nanomaterials (such as ferromagnetic nanoparticles, metallic nanoparticles and carbon nanotubes) are capable of hyperthermia therapy for tumor treatment. However, all these materials have variable degrees of toxicity. NDs have been reported to be used in hyperthermia for tumor treatment due to their good biocompatibility. *Vervald et al*. have carried out a series of studies exploring boron doped NDs for hyperthermic applications. It has been established that boron-doped NDs were extremely promising for carrying out hyperthermia and thermos ablation of tumors [20].

Although several reviews have covered synthesis and applications, research on NDs in nanomedicine is still in its infancy and some challenges need to be solved for practical applications as stated below [13]. First, although some progress has been made in synthesizing NDs with controllable sizes, much effort is still needed. NDs with size less than 10 nm and high efficiency fluorescence imaging are important to enter the cell for biomedical applications. Secondly, the convenience of spin and long coherence time make the NV color center very attractive and deeply studied. However, how to effectively control the fluorescence of NV center and to understand the behind regulation mechanism needs to be further explored. Also, it is particularly important to study what causes NDs to agglomerate, and how to prevent the aggregation of NDs after entering the cell. Precision drug loading of NDs and the delivery efficiency requires further research efforts. Finally, Assessment of biocompatibility and toxicity of NDs should be extended to multiple types of cells. Further research is needed to understand their possible effects on the design of biocompatible NDs to meet the requirements of safe nanomedical applications.

4) PARTICLE IMAGING VELOCIMETRY

4.1) Introduction to PIV

Particle Image Velocimetry (PIV) is an optical measurement technique where the velocity field of an entire region within the flow is measured simultaneously [15]. A main advantage of PIV is that it is a quantitative non-invasive flow field mapping technique that can provide physical insight into the overall flow behaviour. PIV facilitates both the extraction of measurement data and the visualization of flow structures.

The newness and great advantage of PIV are that it delivers high resolution flow velocity vector information of a whole plane in the flow in one time [14]. PIV has given new impulse to fluid dynamics research, specifically with focus on unsteady flows that were difficult to map instantly beforehand. PIV has been developed in the fields of fundamental and applied fluid dynamics research and mechanical engineering. Due to its non-intrusive character, PIV can be characterised as an ideal tool for studying animal-generated flows, restricting disturbances and thereby non-natural behaviour to a minimum.

2D-PIV can be defined as 'Mapping of average displacements of groups of tracer particles over a short time interval in a fluid flow by correlating sub-images of two successive images of one illuminated plane of that flow' [16]. In essence, 2D-PIV requires a flow seeded with particles, bright illumination of one plane of that flow and imaging of the particles in the plane. Successive or double exposed images are analysed for displacements of groups of particles to derive vector flow fields. Flow fields can be post-processed to derive additional parameters describing, the local character of the flow. A generalised PIV set-up is shown in Figure 12.

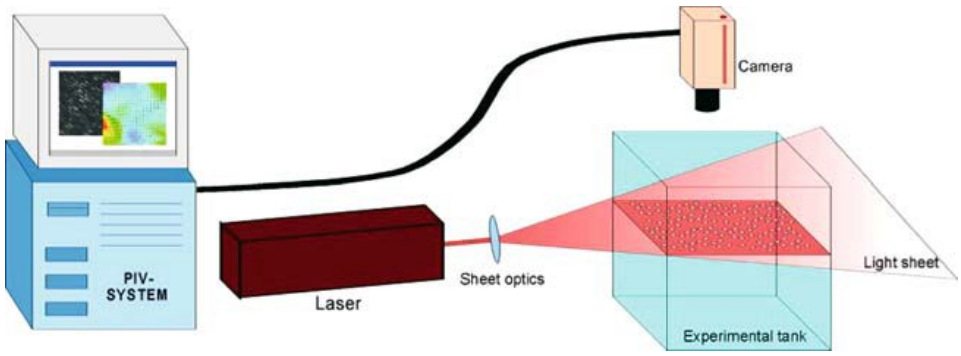

Figure 11: Diagram of a generalised PIV setup showing all major components: the experimental tank with the particles seeded fluid; a laser producing a light sheet that illuminates only one plane in the fluid; a camera imaging the particles in the sheet in the area of interest; a PIV system that analyses the images to derive a vector representing the flow field [12].

To find displacements of groups of particles over a short time interval, two successively recorded images are compared. A small sub-area of the first image, usually called interrogation areas (IA), is compared with a sub-area at the same location in the second image using a cross-correlation technique (Figure 13). This results in the most probable displacement vector for that specific particle pattern (Figure 14). To obtain accurate velocity measurements, each interrogation region should contain many particle-image pairs [17]. Because the displacement is greater than the mean spacing between particle images, it is almost impossible to find individual matching pairs. Therefore, a statistical method, usually correlation analysis, is used to acquire the particle displacement. By computing spatial auto-correlation for double-exposure single-frame images or cross-correlation for double-exposure double-frame images, the location of the displacement correlation peak yields the average particle displacement. In specific case of auto-correlation analysis, the two peaks centred around the self-correlation peak are the "true" displacement-correlation peaks and a 180-degree directional ambiguity occurs due to the symmetry of the auto-correlation.

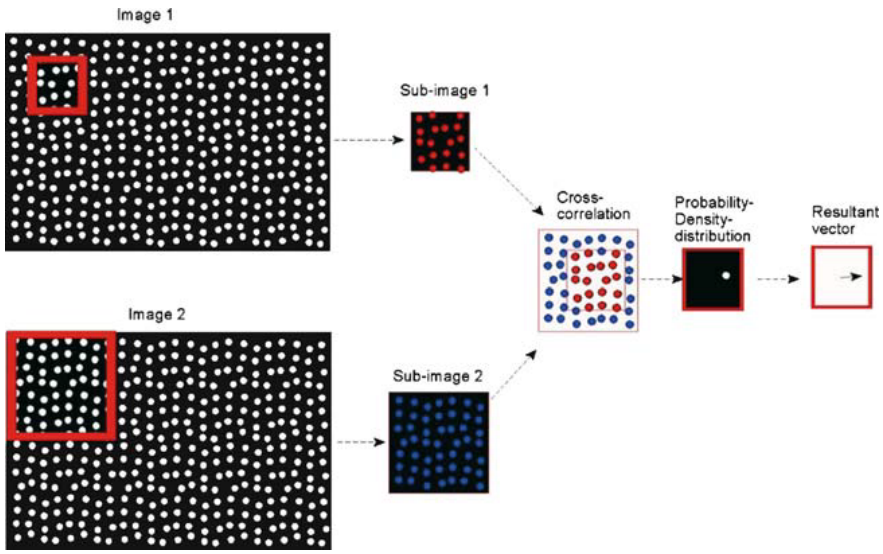

Figure 12: Diagram of the steps in PIV analysis of successively recorded particle patterns in a flow: two sub-images from the same location of two frames are compared in a cross-correlation procedure, resulting in a 2D probability density distribution which shows a peak at the most probable displacement. The peak is located with high precision and a velocity vector, representing the average displacement of the particles in sub-image 1 compared to sub-image 2 is calculated [14].

In case of cross-correlation, there is only one peak, the "true" displacement-correlation peak, and no directional ambiguity needs to be resolved (Figures 15-16). Repeating this procedure for all the interrogation spots and dividing the displacement with the time delay between the two recordings produce a raw velocity vector field. Applying validation algorithms to the raw vector maps, erroneous vectors are detected and removed. Further

analysis of these validated vectors will produce streamlines, vorticity, stress, turbulence intensity etc. The process is repeated for all interrogation areas of the image pair resulting in a complete vector diagram of the flow studied.

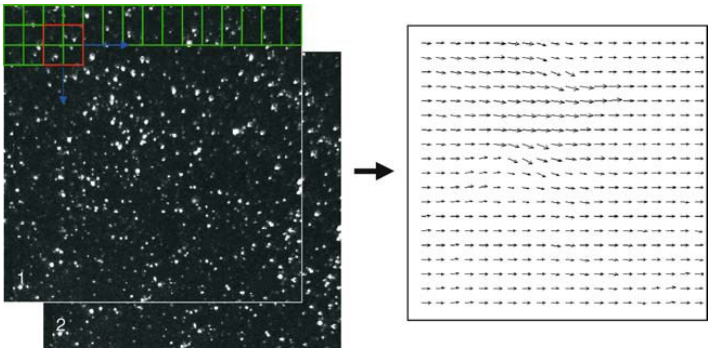

Figure 13: A set of two successive images is analysed by repetitive sampling and subsequent PIV analysis, often with overlap between neighbouring interrogation areas (in this example the overlap is 50% of the interrogation area size in X and Y direction) to get an accurate result without over- or under-sampling [14].

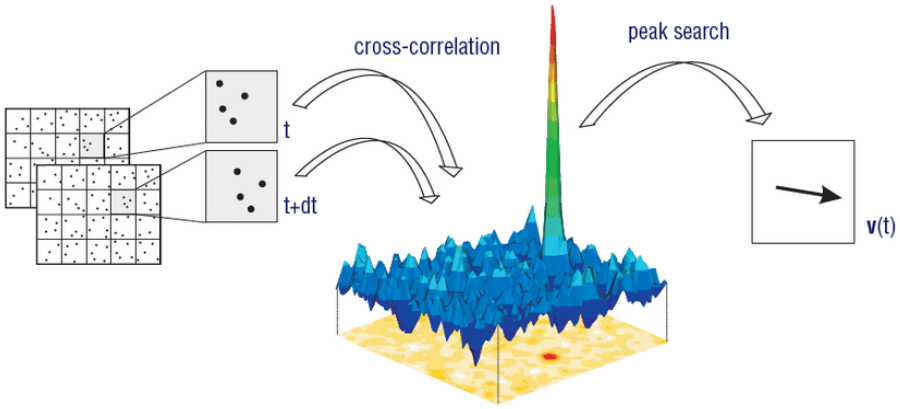

Figure 15: Block-matching cross-correlation technique typically used in PIV. The position of the highest peak in the correlation plane indicates the most likely displacement vector [18].

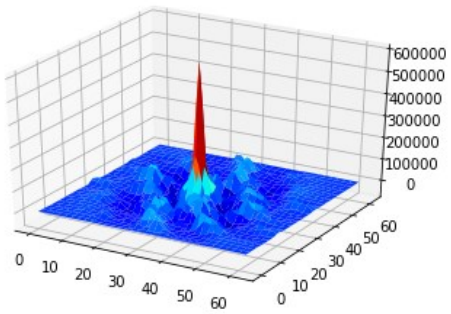

Figure 16: Example of most probable shift vector for PIV image analysis using cross-correlation peak evaluation [19].

4.2) PIV principles

Type of flow

Particle image velocimetry can be applied virtually to any kind of flow, as long as the fluid is transparent to enable imaging of suspended particles [15]. The fluid may be moving, as in a flow tank or wind tunnel, or standing still, as in an aquarium where an organism itself is moving. The fluid may be liquid or gaseous.

Seeding

To visualise flow for PIV purposes, the fluid has to be seeded with particles. To follow flow accurately, these particles need to be neutrally buoyant (neither sink nor rise) and small enough with respect to the flow phenomena under investigation [15]. The typical particle size for fluid flow applications ranges from 5 to 200 μm, depending on flow speed and camera magnification. For biological applications, the particles should not be toxic, or clog up the respiratory structures of the organisms involved. In all cases the particles should preferably be highly reflective, to yield good particle images on the PIV recordings.

Illumination

In PIV flow studies, illumination is usually provided by a laser light sheet. A narrow sheet of light is used to define the plane of investigation [15]. A laser is used because it can deliver a bright sheet with almost constant thickness without aberration or diffusion, due to the coherent and monochromatic character of the emitted light. This results in a sheet with a slightly converging thickness, enabling the experimenter to select a certain sheet thickness tuned to the experimental conditions. The types of lasers used for PIV illumination can be divided in two categories: continuously emitting lasers, usually called CW (= continuous weight) lasers, and pulsating lasers.

Imaging

The illuminated plane in the particle seeded flow is visualized by a camera with its optical axis perpendicular to the plane, in order to record the whole plane in focus [15]. High quality lenses are generally necessary because the light levels are usually relatively low and large apertures have to be used. In normal 2D-PIV, a black-and-white (B/W) camera suffices. Experimental characteristics such as event speed, repeatability and illumination intensity need to be evaluated in order to choose a camera for a specific application, often in combination with the illumination system.

PIV analysis

The principle of PIV-analysis of a pair of images recorded successively from one illuminated plane of a particle seeded flow is depicted in Figure 13. The steps in the analysis process are: (1) selection of interrogation areas or sub-images for analysis, (2) correlation analysis, (3) finding the displacement peak, (4) calculating the velocity vector, and (5) repeat for next set of sub-images (back to 1) [15].

For the pre and post-analysis of the collected images, several parameters are essential for the correct evaluation of the fluid flow. Before recording the images it's necessary establish the right amount of time passing between two different frames (Δt), which has to be decided depending on the characteristics of the analysed flow (velocity, density, physical parameters that influence the movement). Later on, for post processing of recorded images, it is important to set the percentage of border overlapping of the cross-correlation algorithm, permitting a proper trajectory calculation, considering all possible displacements of the particles contained into the sequential frames, even the ones not inside the analysed ROI for the vector tracing.

5) STUDY

5.1 Aim of the study

The study is aimed to establish if, given a photoluminescent Nanodiamond powder, would be possible to detect its particles in a stream flow coming out from an airbrush, using a PIV system for the scope. The purpose of this hypothesis is to verify whether the detection results easier when exciting the NDs and visualizing them in the collected picture.

5.2 Procedure and data collection

5.2.1 Material characterization

The first step of measuring procedure is characterization of material and samples. During the experiment two different types of NDs have been used:

a) RT-DND: Nanodiamond powder of detonation synthesis, purified, graphite and metal free, non-modified. Average grain size: 3.5-6.0 nm, ash residue: <0.1 wt.%, polydispersed (heterogeneous in size) (Figure 17).
   Manufactured for many different biomedical applications such as bioimaging, cell tracking, etc [23].
b) RT-DND-LN: Detonation nanodiamond powder, purified, nitrogenized. Average grain size: 3.5-6.0 nm, high photoluminescence, hydrophobic and lyophobic, ash residue: <0.1 wt.% (Figure 18).
   Manufactured for metal and ceramic composites, nuclear applications [23].

Figure 17: RT DND reference container

Figure 18: RT DND LN reference container

Carbon nano-powder are in solution with distilled water (50 mg in 50 ml). It can be seen that the two different kinds of NDs have different colour and show different hydrophobicity when mixed with water (the nitrogenized NDs seem to have a higher hydrophobic behaviour: it is difficult to dissolve the bigger conglomerates). Due to the production process of these NDs the nano particles are never perfectly separated and tend to join in bigger agglomerates of a size close to 100 nm, too big for our project. To solve to this problem, samples have been subjected to a sonication procedure to break up the bigger agglomerates into the average smaller size for the NDs. (Equipment: Omni Sonic Ruptor 400 Ultrasonic Homogenizer [24], sonication time = 30 minutes at 160 W 20 kHz). At the end of the process the RT-DNDs showed a higher solubility in water whereas the RT-DND-LN remain less mixed and more agglomerate together but still small enough to the aim of the project. Figures 19 and 20 show the set for the sonification homogenization procedure and the result for the samples.

Figure 19: Sonication homogenization prodecure

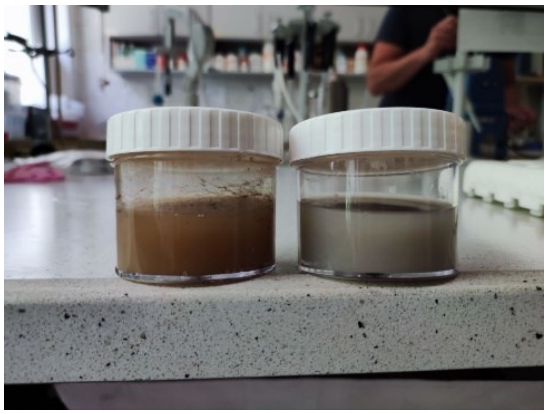

Figure 20: Final sample product: Left RT-DND-LN, Right RT-DND

Another necessary characterization is the entity of scattered light from the NDs, using Raman spectroscopy technique.

Raman spectroscopy is an analytical technique where scattered light is used to measure vibrational energy modes of a sample [25]. Raman spectroscopy can provide both chemical and structural information, as well as the identification of substances through their characteristic Raman 'fingerprint'. Raman spectroscopy extracts this information through the detection of Raman scattering from the sample (Figure 21). When light is scattered by molecule, oscillating electromagnetic field of a photon induces a polarisation of the molecular electron cloud which leaves the molecule in a higher energy state with the energy of the photon transferred to the molecule. This can be considered as the formation of a very short-lived complex between photon and molecule, which is commonly called virtual state of the molecule. This virtual state is not stable and the photon is re-emitted almost immediately, as scattered light.

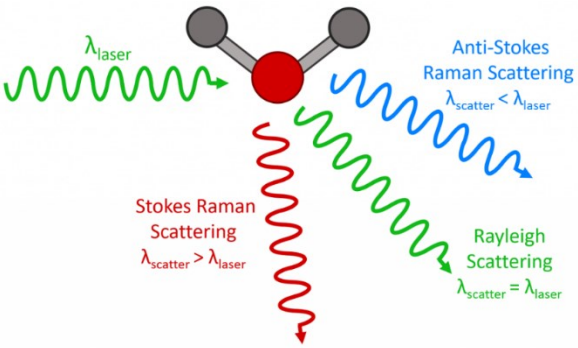

Figure 21: Three types of scattering processes that can occur when light interacts with a molecule.

In most scattering events, the energy of the molecule is unchanged after its interaction with the photon; the energy, and therefore the wavelength, of the scattered photon is equal to that of the incident photon [26]. This is called elastic (energy of scattering particle is conserved) or Rayleigh scattering and is the dominant process. In a much rarer event (approximately 1 in 10 million photons) Raman scattering occurs, which is an inelastic scattering process with a transfer of energy between the molecule and scattered photon. If the molecule gains energy from the photon during scattering (excited to a higher vibrational level), then the scattered photon loses energy and its wavelength increases, which is called Stokes Raman scattering (after G. G. Stokes).

Inversely, if the molecule loses energy by relaxing to a lower vibrational level, the scattered photon gains the corresponding energy and its wavelength decreases: a

phenomena named Anti-Stokes Raman scattering. Quantum mechanically Stokes and Anti-Stokes are equally likely processes. However, with an ensemble of molecules, most molecules will be in the ground vibrational level (Boltzmann distribution) and Stokes scatter is the statistically more probable process. As a result, the Stokes Raman scatter is always more intense than the anti-Stokes and for this reason, it is nearly always the Stokes Raman scatter that is measured in Raman spectroscopy (Figure 22).

Figure 23a depict the graph showing our results for RT DND and RT DND LN nanodiamonds.

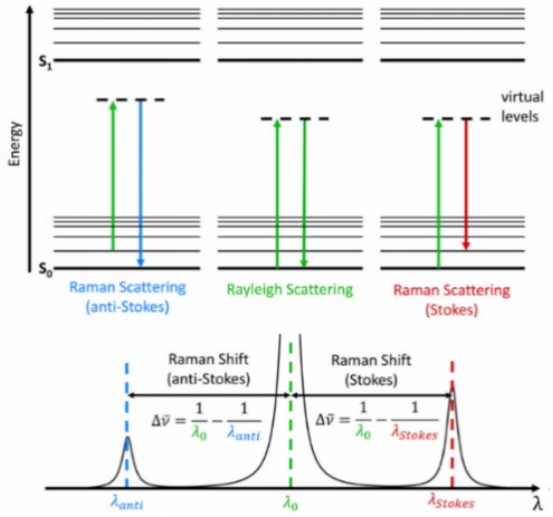

Figure 22: Jablonski Diagram showing the origin of Rayleigh, Stokes and Anti-Stokes Raman Scatter

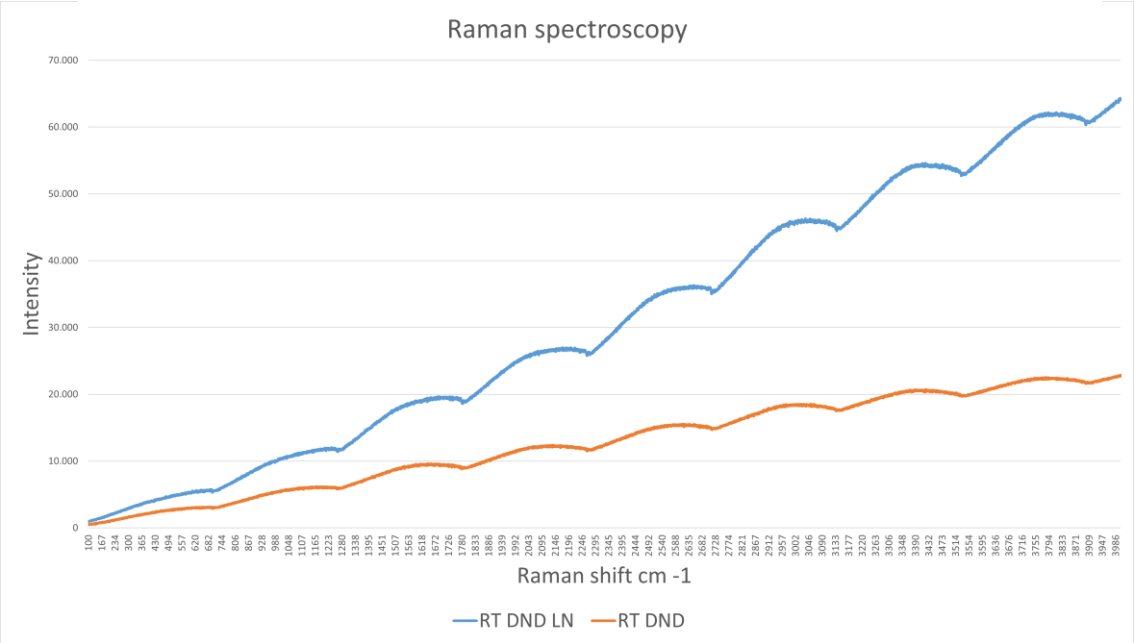

Figure 23 a: Raman spectroscopy results for NDs samples

It is easy to notice that the graph is not readable as normal, due to photobleaching and photoluminescence of the NDs. As the samples show a high luminescence when exposed to some specific laser wavelength, it was not possible to get any information or relevant data from the Raman measurement. Figure 23b and 23c show the expected Raman

spectroscopy graph for pure NDs (with the typical peak at 1380 cm^{-1} for pure diamond) and for doped NDs (still present the peak at 1380 but other peaks can be spotted in the spectra) [37].

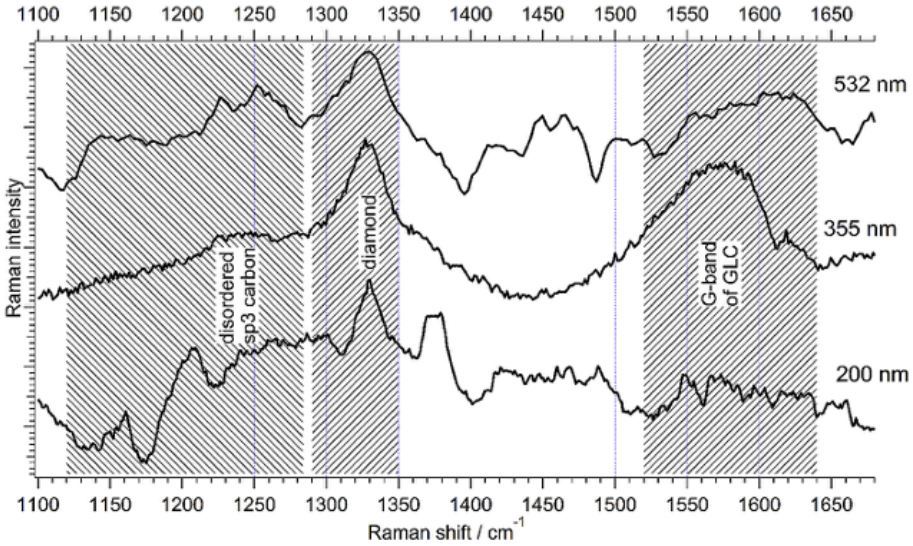

Figure 23 b: Experimental Raman spectra of 3 nm DND at different excitation wavelengths; the major bands of different carbon phases highlighted

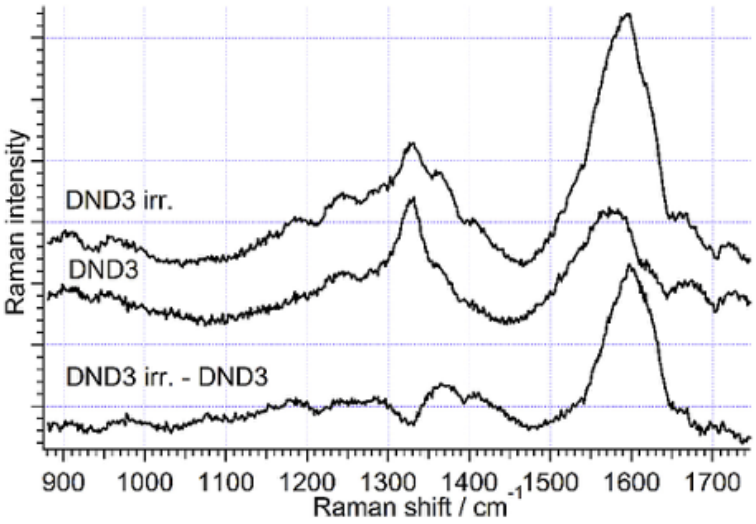

Figure 4: The effect of nitrogen ions irradiation on the ND structure: Raman spectra under 355 nm excitation of irradiated sample (top), original sample (middle), and the difference (bottom).

As further step in the sample characterization, luminescence measurement has been carried out for the two types of NDs. The luminescence spectra have been studied using two different excitation wavelengths for both samples (430 nm as first excitation and 530 nm as main excitation wavelength for the NDs). Secondly, the excitation broadband has been detected to check the actual behaviour to the entire range of wavelength. For all measurements, samples have been placed on a Teflon tray (the luminescence spectra have been studied for the tray as well for being sure to not have any influence on the sample spectra). Figure 24 shows the Teflon spectrum, Figures 25 and 26 show the luminescence emission spectra for the samples using 430nm and 530 nm as excitation wavelength, respectively.

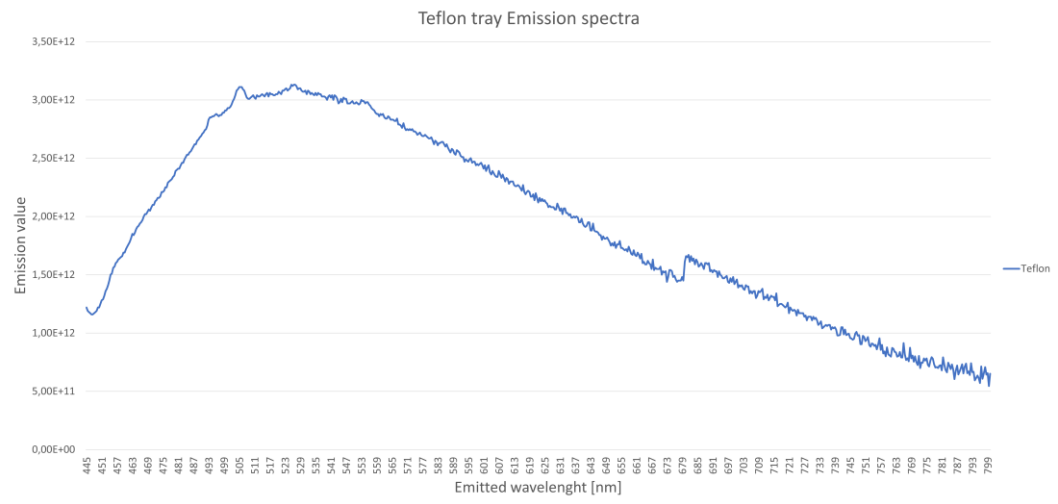

Figure 24: Teflon luminescence emission spectrum

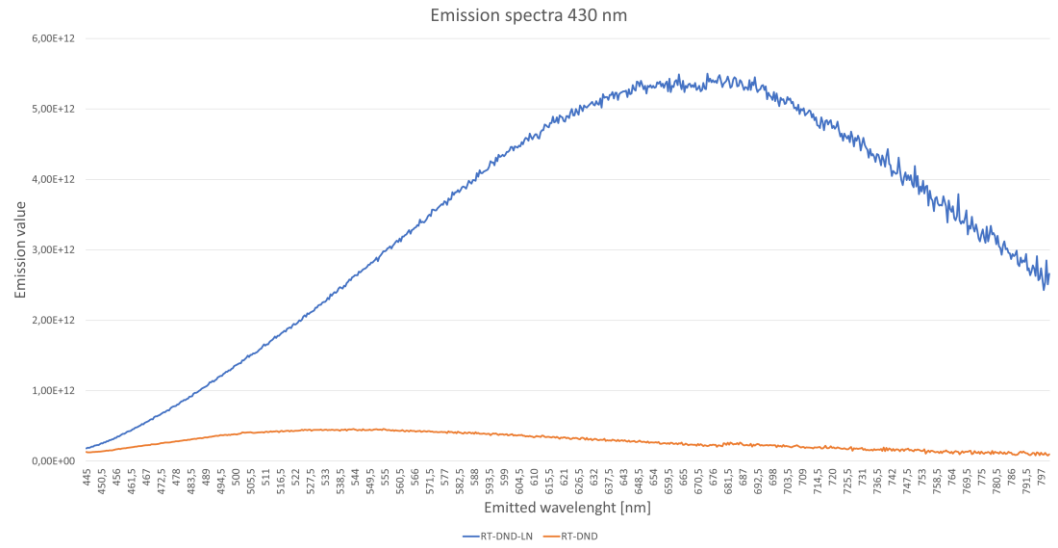

Figure 25: Luminescence emission spectrum for 430nm

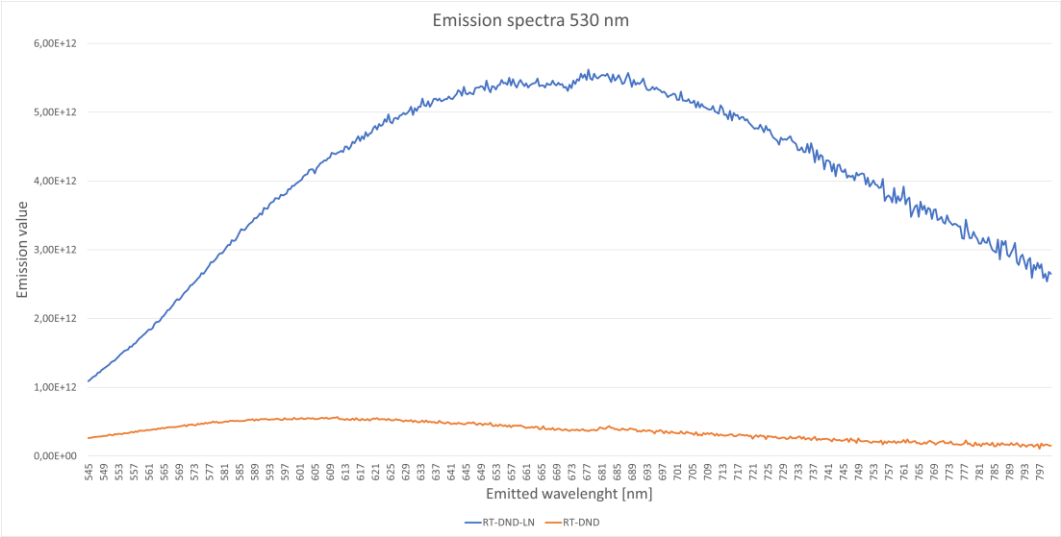

Figure 26: Luminescence emission spectrum for 530nm

From the graphs it is possible to state that the Teflon tray has no influence on the NDs spectra. It is worthy to pinpoint how the nitrogenized NDs (RT DND LN) have a much stronger response in terms of luminescence emission than the unmodified nanodiamonds. Both the NDs samples anyway show a great luminescence emission in the range of 630-700 nm if excited with the proper wavelength. The value of maximum luminescence is found coherent with the literature on NDs photoluminescence [27].

For a wider view about the luminescence behaviour of the NDs, excitation broadband scansion has been made. From luminescence spectra of the samples the wavelength with the higher luminescence value was picked: 550 nm for the unmodified diamonds (RT DND) and 675 for the nitrogenized diamonds (RT DND LN). The results are shown in Figures 27 (compared) and 28 (normalized), respectively. For both the analysed sample the centre of the broadband is around 480 nm, in coherence with the common diamond properties that the samples share. The modified diamonds possess a wider broad spectrum with a constant response to a vast range of excitation wavelength (from 350 nm to 600 nm). The broad spectra, as result, evidence the semiconductor properties of NDs [28]

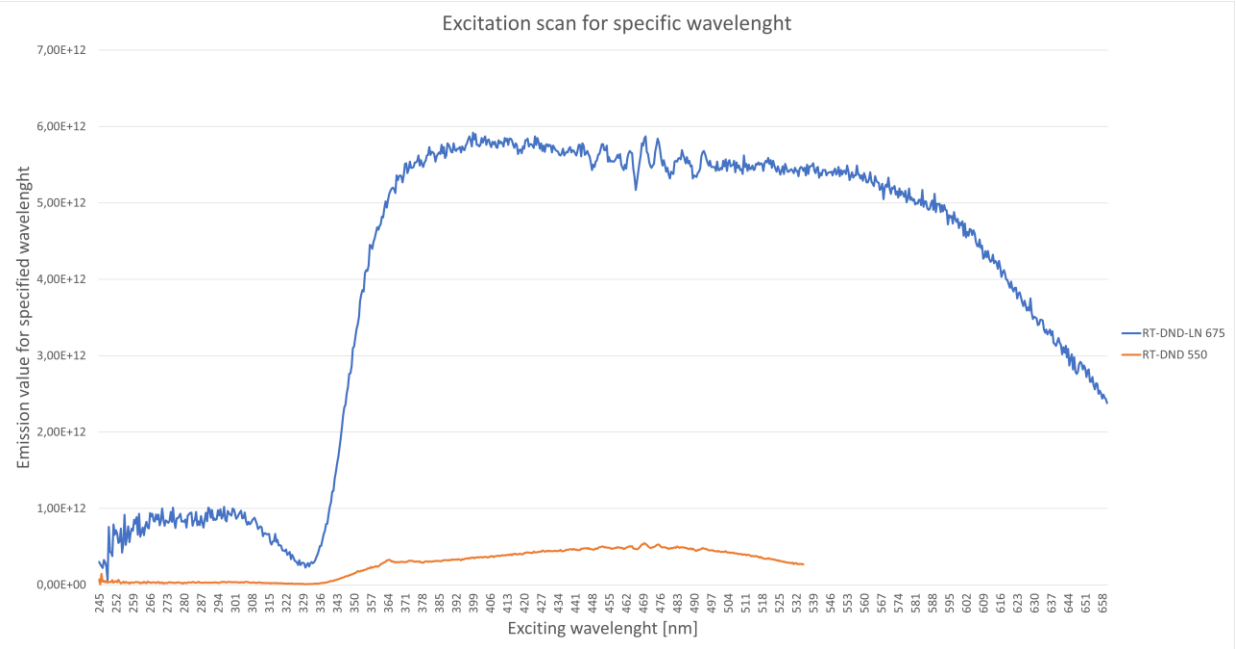

Figure 27: Excitation broad spectrum for RT DND at 550 nm

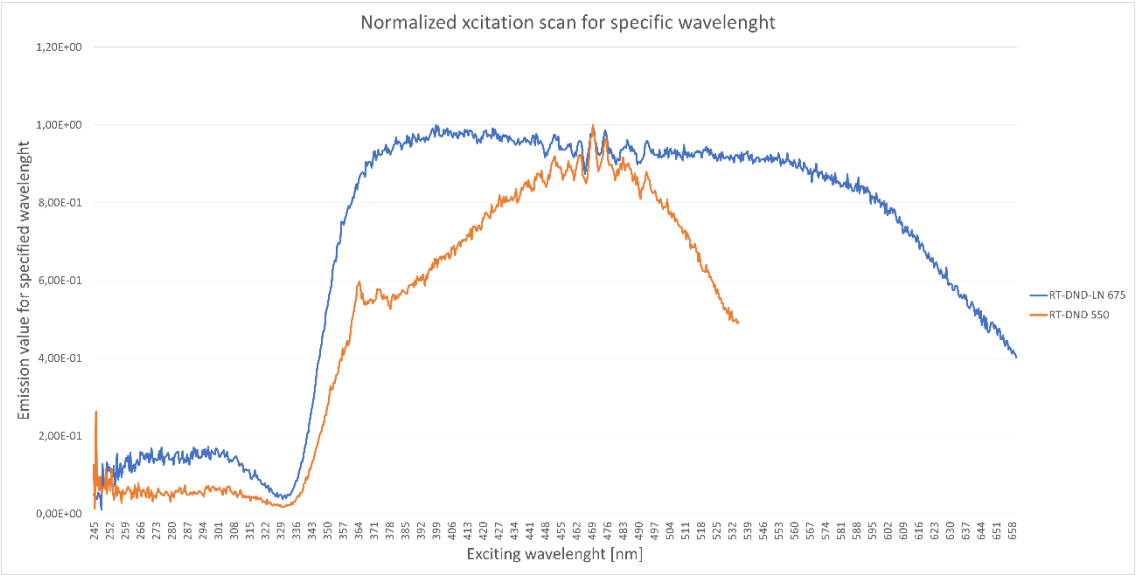

Figure 28: Excitation broad spectrum RT DND LN at 550 nm normalized

For Raman Spectroscopy measurement the used equipment was the Raman micro-spectrometer T-64000 (Jobin- von), equipped with the microscope BX-40 (Olympus) [29] For luminescence spectra analysis the equipment used was the FLS 980 Spectrometer (Edinburgh Instruments) [30]

5.2.2 PIV images acquisition

Next step was to set up the structure of the PIV equipment (camera, laser, laser plane, airbrush). Figure 29 show the spatial disposition of every part of the structure and following a specific description of the equipment along with technical features.

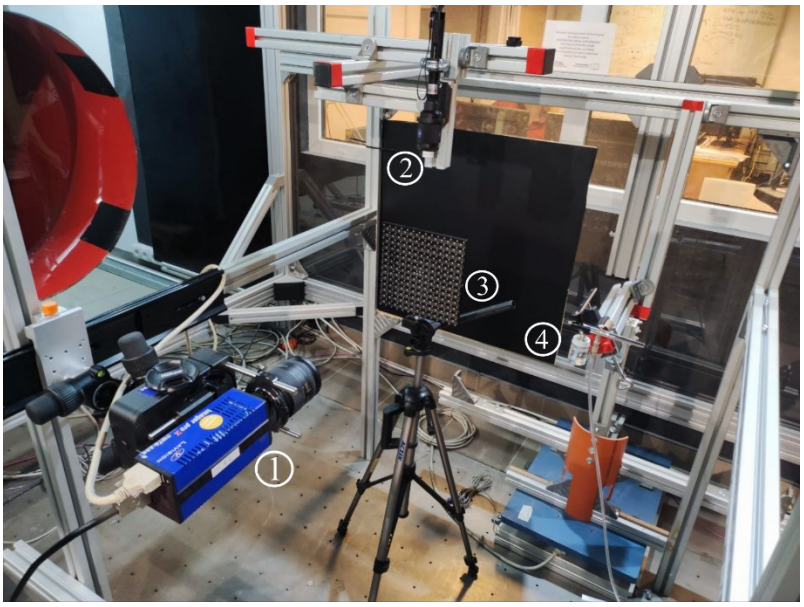

Figure 29: PIV equipment set up inside the laboratory: 1) High speed camera, 2) Green pointer laser with lens for laser plane, 3) calibration plate for laser plane, 4) airbrush for NDs particles dispersion

Camera

LaVision Imager pro X 4M is a high sensitivity, high resolution digital camera used in the LaVision FlowMaster PIV system. This camera is equipped with an interline transfer chip with progressive scan readout and up to 4 GB memory in the camera head to store more images faster than any interface to a PC can currently handle. It mounts a Nikon lens IF aspherical Macro (1:2) 72 mm diameter 2.8 focal [31].

Laser

Due to some driver fails occurred, the original LaVision PIV laser could not be used, so L303 green pointer laser, mounted above the splitting lens that will form the laser plane was used in alternative. It has a wavelength of 532 nm with 60 w of power [32] making it an adeguate candidate for the porpuse.

Calibration plate

The calibration plate is an essential tool for the optimal calibration of the software regarding distance between the laser and the camera, focus of the camera on the laser plane, verification laser plane perpendicularity respect the ground and the camera lens and the check the eventual presence of some distortion due to the lens. Here the LaVision calibration plate type 22 has been used (distance dot-dot of 15 mm) [33]. Figure 30 shows the right positioning of the plate with the laser plane

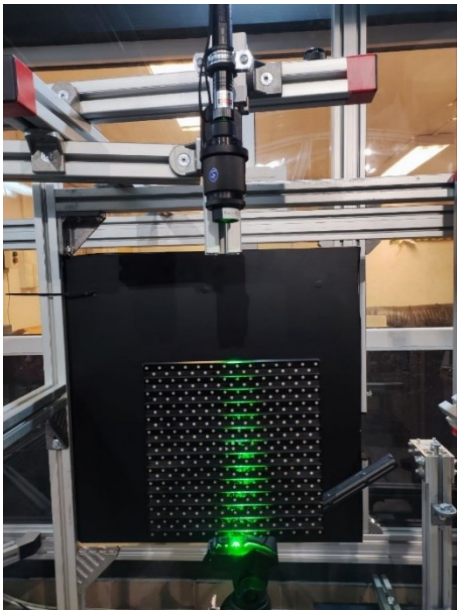

Figure 30: Correct calibration plate position respect the laser plane

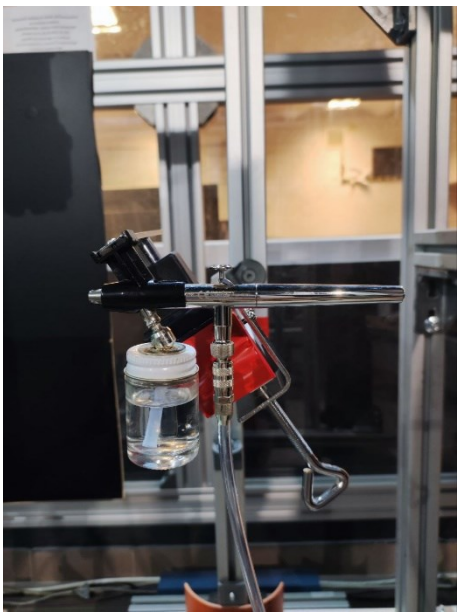

Figure 31: Airbrush configuration and position

Airbrush

The ultra X 63318 aerograph from Harder & Steenback is a compressed air aerograph with interchangeable noozle (noozle diameter 0.4 mm, 0.2 mm, 0.15 mm) and pressure thanks to a small air compressor attached to it. It will be the tool creating the stream of particles for the PIV detection [34].

PIV Software

For the calibration, collection of images, and visualization of the results the software LaVision DaVis 10 has been used. Combining high-performance cameras with outstanding image processing algorithms opens new dimensions for imaging applications. DaVis 10 has been redesigned from the ground-up to deliver a software for modern demands for usability, data handling and visualization [35]. Figure 32 present

the main software window. Figure 33 shows all the PIV structure during the images collection.

Figure 32: DaVis PIV software principal window

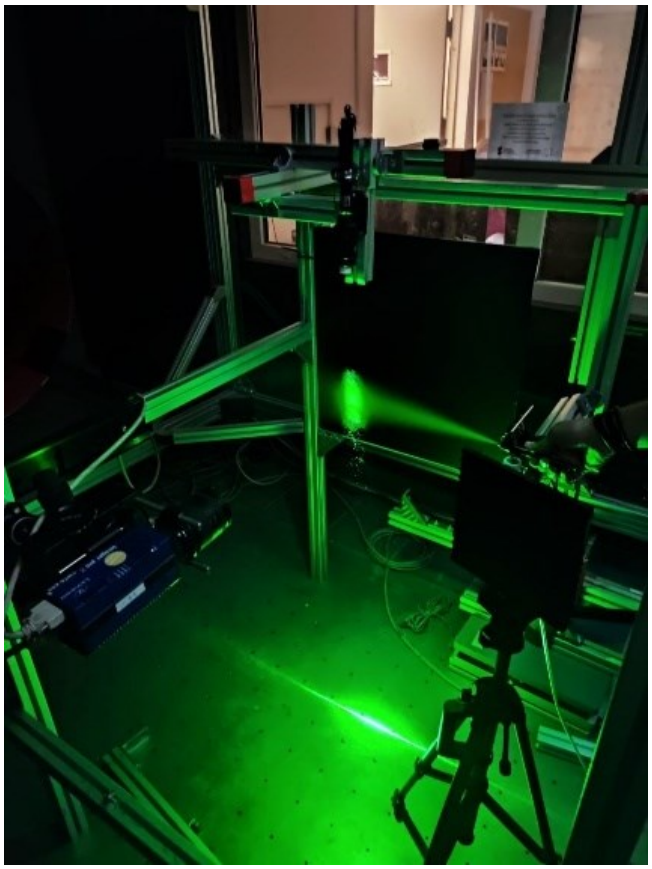

Figure 33: Working PIV system during image collection

For image collection, different configuration has been tested. To have a wide view about the behaviour of the system, the selected parameters are those which permit a visualization of the different possible situations encountered: the exposure time influence the amount of light entering the camera lens, the air pressure changes the velocity with which the particles fly in the air in front of the camera, the number of erogated particle changes with nozzle diameter. Image acquisition was done by the software, with the possibility of applying some pre/post production image processing: all images has been taken applying a Dark image subtraction, some test has been done applying a Background subtraction.

In the Dark image subtraction a dark image is taken with the lens covered by the cap, to have an image of the unchangeable noise added by the camera, image that will be subtracted from the data image for noise reduction. In the Background image subtraction the same process is done, but with the image of the background of the Field of Interest (FOI) of the camera (the black panel visible in Figure 29). For each configuration 10 consecutive images were taken and one out of ten selected for the analysis. After Table 4 summarize the configurations used for the water sample.

Table 4: Water sample tried parameters configuration. The blue squares indicate the tried configuration.

Demineralized water		**Exposure time [ms]**											
		100	200	300	400	500	600	700	800	900	1000	5000	10000
Airbrush configuration	N.D 0.4 mm P. 100 kPa												
	N.D 0.4 mm P. 140 kPa												
	N.D 0.4 mm P. 180 kPa						WaW B.S.				WaW B.S.		
	N.D 0.2 mm P. 180 kPa												

Legend:
N.D. = Noozle diameter **P.** = Aerograph air pressure
WaW B.S. = With and without Background Subtraction
B.S. = Only with background subtraction

Each image has been renamed by the configuration parameters used for it. Following an example of the name with explanation:

W_N04_T1000_P180_L28_LOFF_BS_05072022_1

W = water (sample)
N04 = nozzle diameter equal to 0.4 mm
T1000 = camera exposure time equal to 1000 ms
P180 = air pressure equal to 180 kPa
L28 = lens opening focal equal to 2.8
LOFF = test made with the room light turned off
BS = image taken with background subtraction
05072022 = test made on 5th July 2022
1 = first attempt to test

After the water images collection some consideration can be made:
First one is that water particles, if the configuration is optimal, are well visible in the FOI of the camera despite the lower energy of the laser respect the original one and, mostly depending on the exposure time, the particles stream path and single particles are visible.
Following some example images taken with different configurations. Figures from 34 to 39 show images of water stream taken with different nozzle diameters (0.2 mm, 0.4 mm), different air pressure (100 kPA, 140 kPA, 180 kPa) and different exposure time (from 100 ms to 10000 ms at 100 ms width step until 1000 ms, than 1000 ms, 5000 ms, 10000 ms)

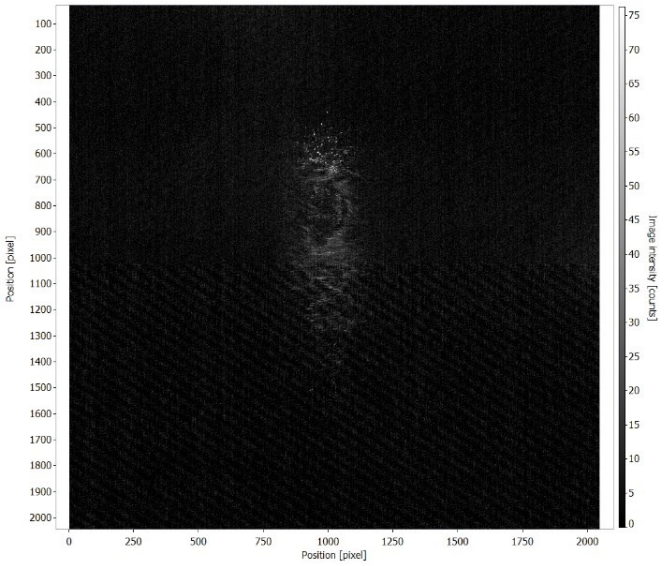

Figure 34: W_N02_T100_P180_L28_LON_05072022_1

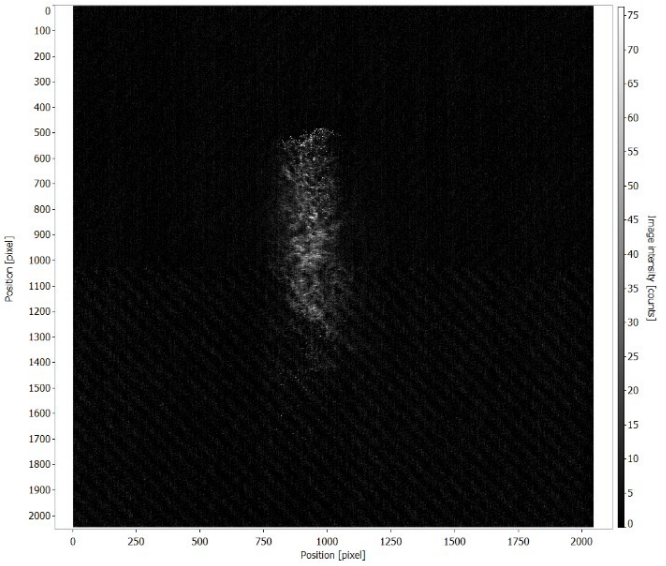

Figure 35: W_N04_T500_P140_L28_LOFF_05072022_1

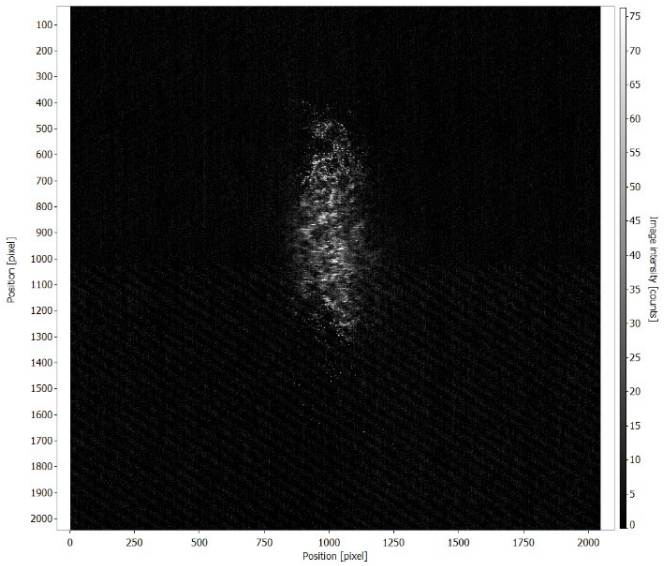

Figure 36: W_N04_T700_P100_L28_LOFF_05072022_1

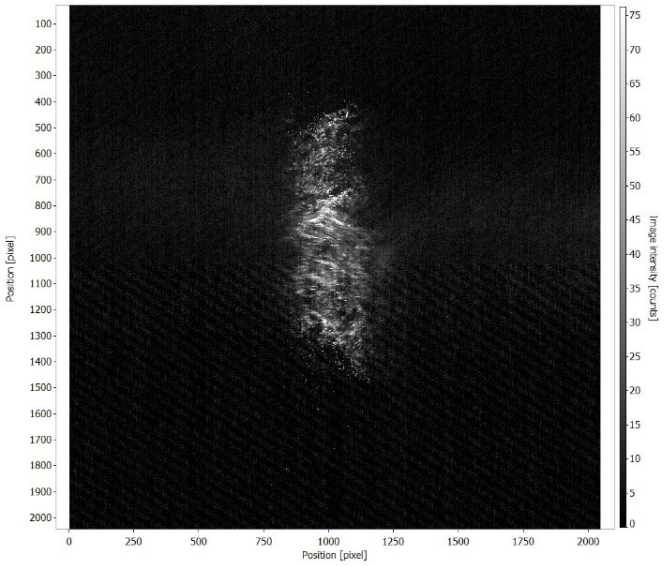

Figure 37: W_N04_T1000_P100_L28_LON_05072022_1

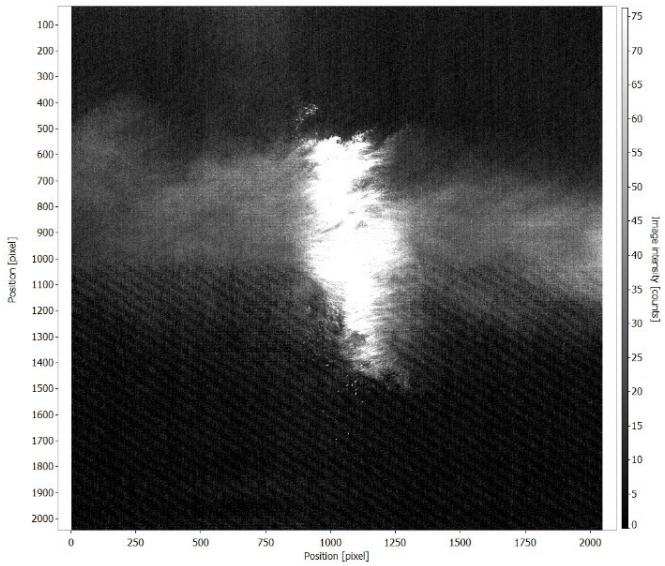

Figure 38: W_N04_T5000_P180_L28_LON_05072022_1

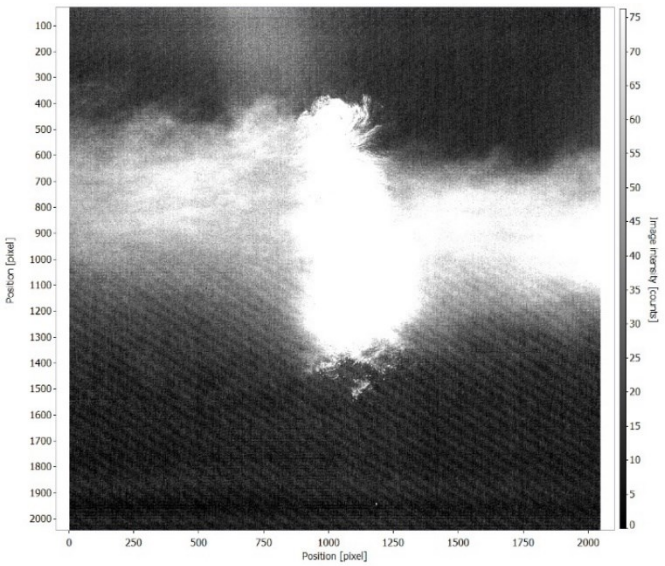

Figure 39: W_N04_T10000_P180_L28_LON_05072022_1

Generally, expectations regarding the influence of the changing parameters can be confirmed when comparing some images:

- A bigger nozzle diameter permits a better erogation of the particles (Figure 40 as comparison).
- A higher exposure time gives brighter and clearer images (NB: to high exposure time = too bright images) due to more light entering the lens, but as consequence it's more likely to evidence the particles paths than the particles themselves.
- A lower air pressure pushes less particles in the air but allows a better visualization of the single particles thanks to the lower velocity (Figure 41 as comparison).
- Lens focal opening is enough to get the proper amount of light. there is some small difference if the test is made with or without the room lights turned off.
- Background subtraction works fine for high exposure time but give too much dark images, with almost impossible to detect particles, if considered in lower exposure time (Figures 42 and 43 as comparison)

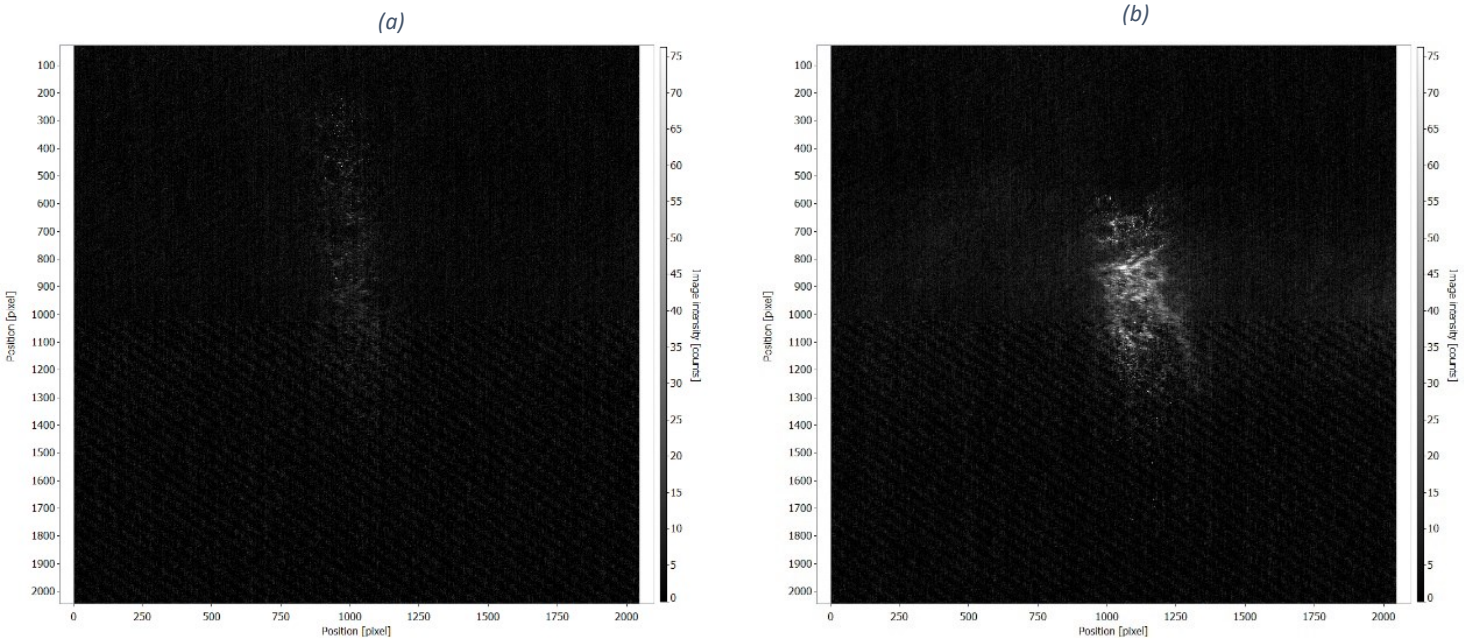

Figure 40: Nozzle diameter behaviour comparison (a) W_N02_T500_P180_L28_LON_05072022_1 (b) W_N04_T500_P180_L28_LON_05072022_1

(a) (b)

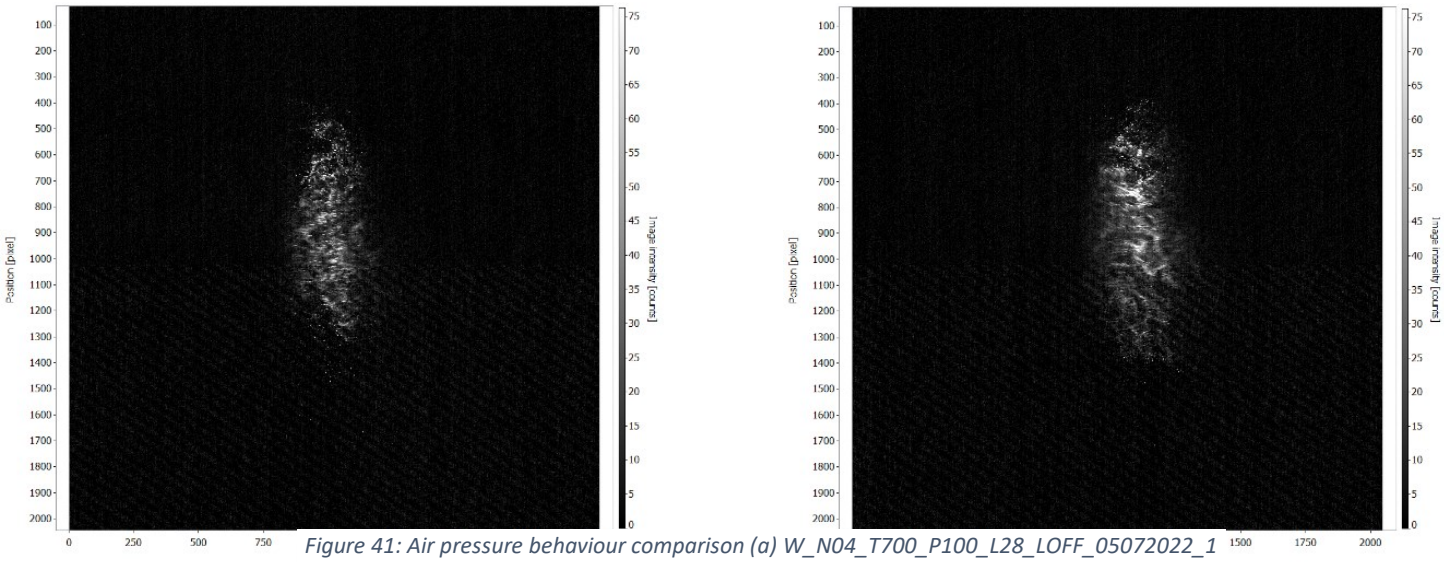

Figure 41: Air pressure behaviour comparison (a) W_N04_T700_P100_L28_LOFF_05072022_1 (b) W_N04_T700_P180_L28_LOFF_05072022_1

(a) (b)

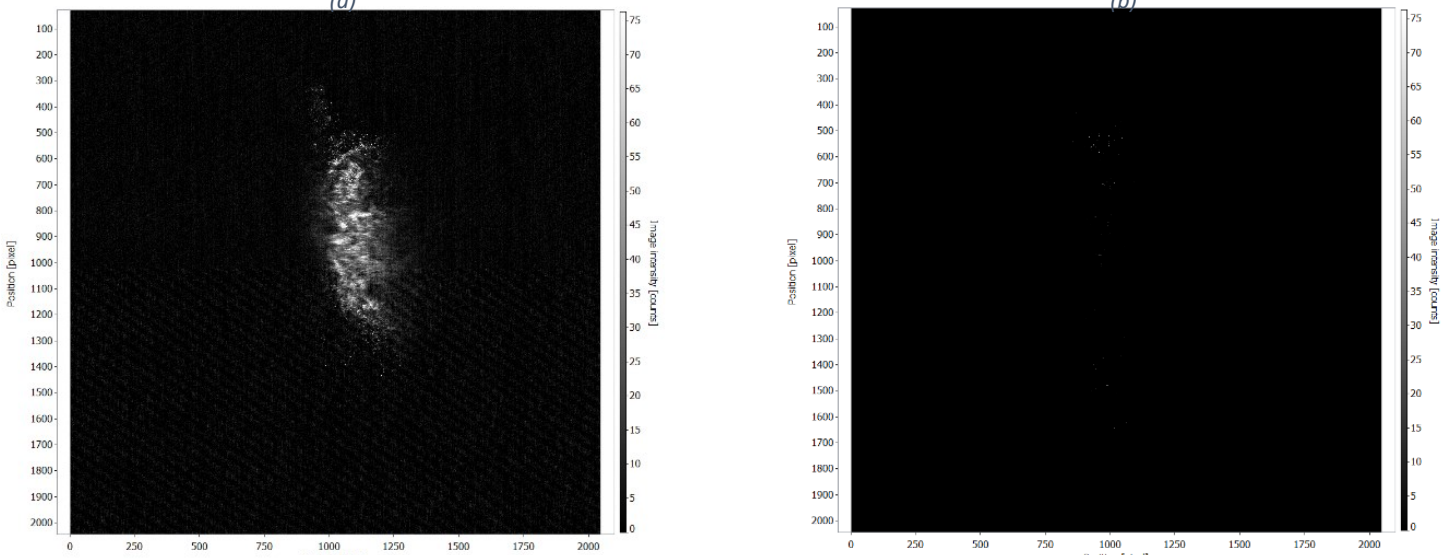

Figure 42: BS Behaviour comparison for T600 (a) W_N04_T600_P180_L28_LOFF_05072022_1 (b) W_N04_T600_P180_L28_LOFF_BS_05072022_1

(a) (b)

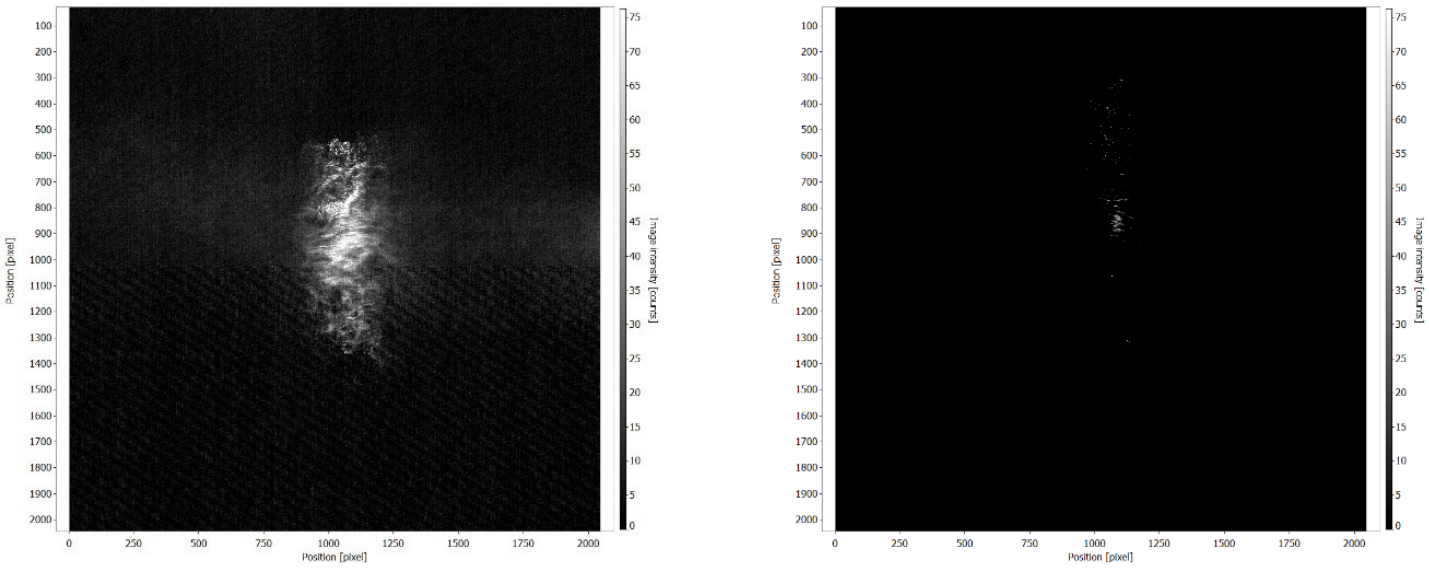

Figure 43: BS Behaviour comparison for T1000 (a) W_N04_T1000_P180_L28_LOFF_05072022_1 (b) W_N04_T1000_P180_L28_LOFF_BS_05072022_1

Before proceeding with the NDs mixtures test some decisions have been made for focusing the image collection on the most interesting configurations for the scope. Therefore, the taken decisions have been to:

1. Reduce the range of exposure time (from 300 to 5000).
2. Make teste for three air pressure: 180 kPa, 100 kPa and 50 kPa (for some ex. time).
3. Keep the principal focus on the 0.4 mm nozzle diameter but make some test anyway with the 0.2 mm nozzle.
4. No test will be made with background subtraction with an exception for high exposure time (1000, 5000)

The image collection procedure and renaming has been kept unchanged from the previous one. Table 5 summarize the configurations used for the NDs mixtures test.

Table 5: Nds sample tried parameters configuration. The yellow squares indicate the tried configuration.

Nanodiamonds sample		Exposure time [ms]								
		300	400	500	600	700	800	900	1000	5000
Aerograph configuration	N.D 0.4 mm P. 50 kPa								WaW B.S.	WaW B.S.
	N.D 0.4 mm P. 100 kPa								BS	BS
	N.D 0.4 mm P. 180 kPa								BS	BS
	N.D 0.2 mm P. 100 kPa								BS	
	N.D 0.2 mm P. 180 kPa								BS	

Legend:
N.D. = Noozle diameter **P.** = Aerograph air pressure
WaW B.S. = With and without Background Subtraction
B.S. = Only with background subtraction

Following some example images taken with different configurations for both the NDs sample mixture (RT-DND left, RT-DND-LN right).

Figures 44 and 45 show Images taken with 0.2 mm nozzle diameter

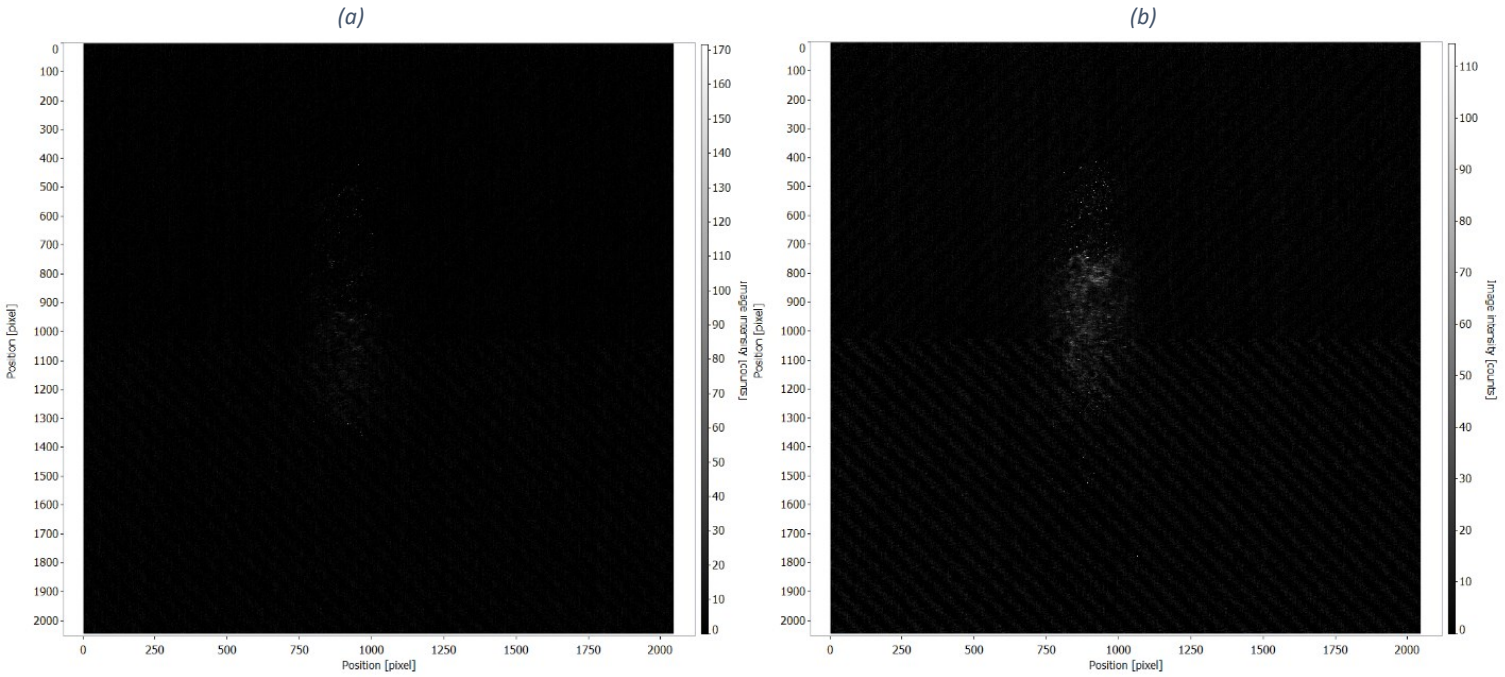

Figure 44: (a) RTDND_N02_T500_P180_L28_LOFF_06072022_1
(b) RTDNDLN_N02_T500_P180_L28_LOFF_06072022_1

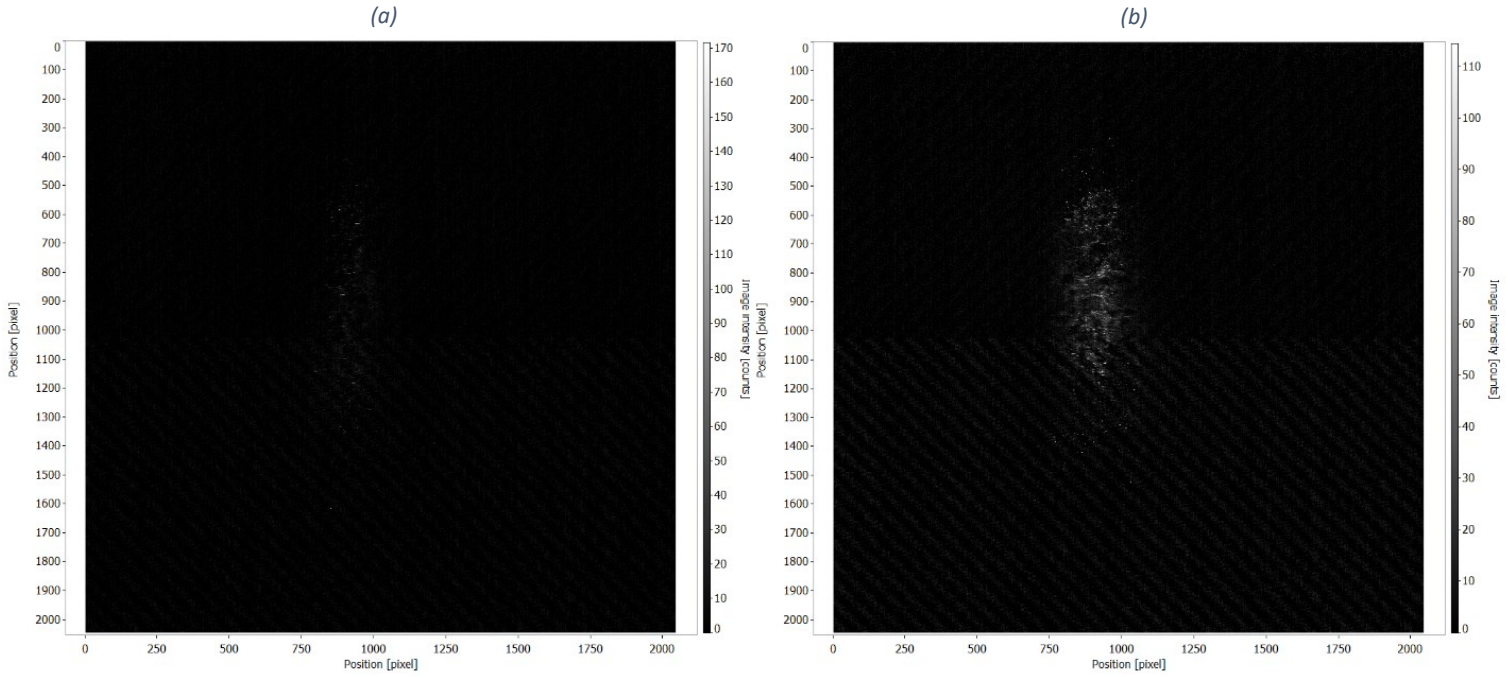

Figure 45: (a) RTDND_N02_T700_P180_L28_LOFF_06072022_1
(b) RTDNDLN_N02_T700_P180_L28_LOFF_06072022_1

Figures from 46 to 56 show images taken with 0.4 mm nozzle diameter changing the air pressure (100 kPa, 180kPa, 50kPa) and the exposure time (increasing order).

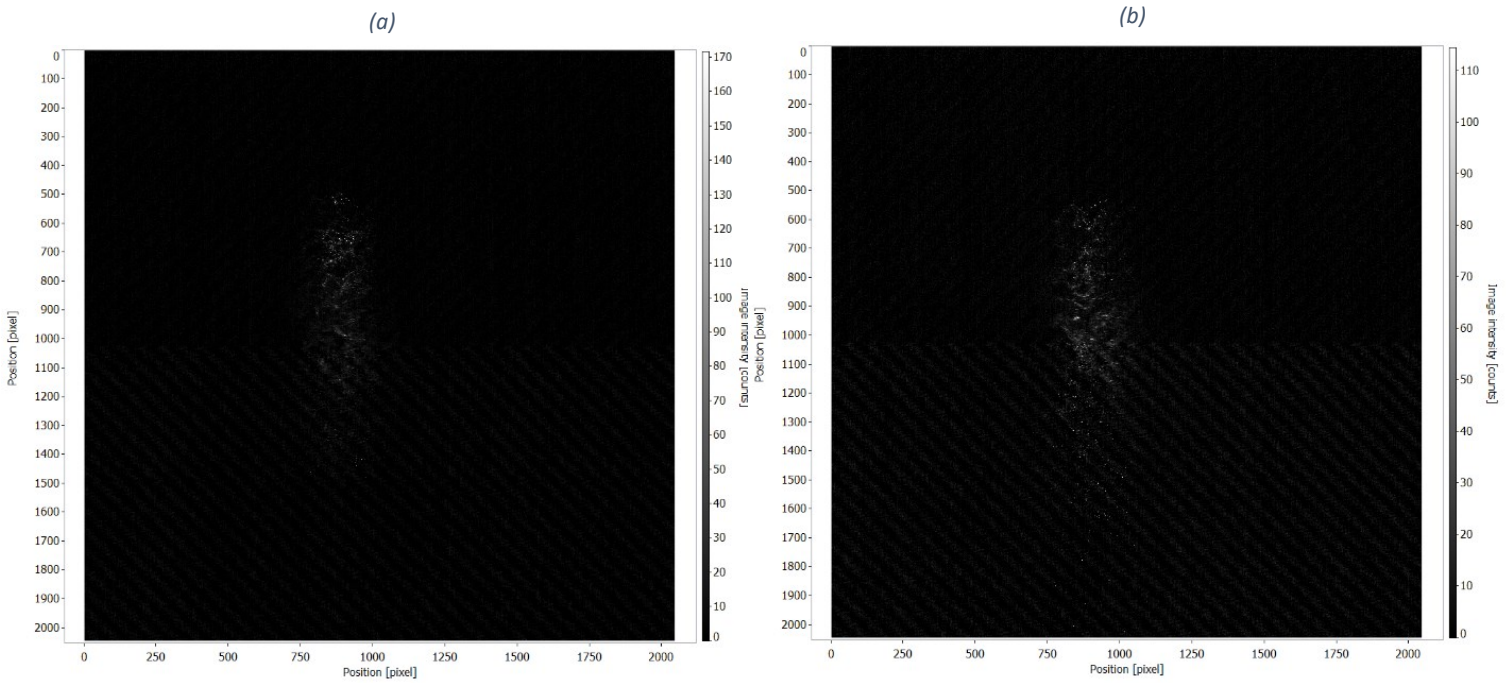

Figure 46: (a) RTDND_N04_T400_P100_L28_LOFF_06072022_1
(b) RTDNDLN_N04_T400_P100_L28_LOFF_06072022_1

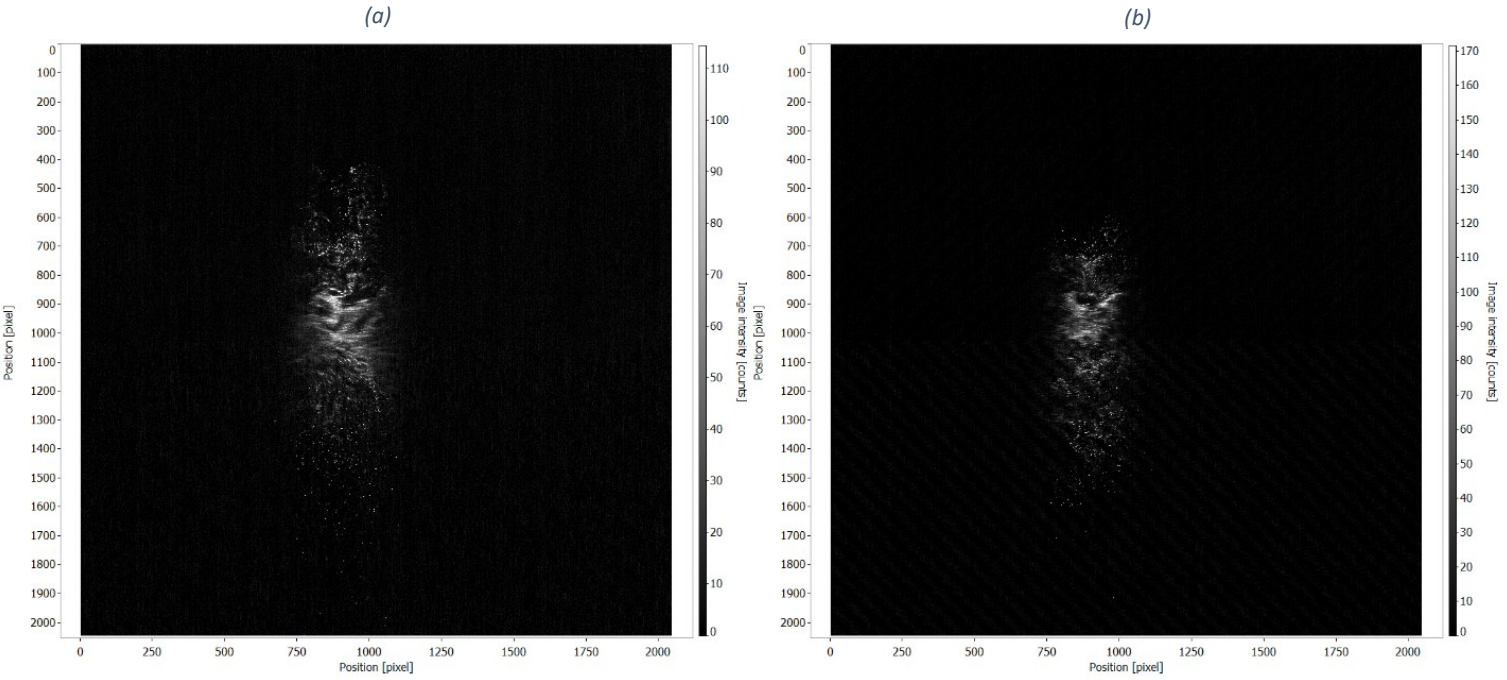

Figure 47: (a) RTDND_N04_T1000_P100_L28_LOFF_06072022_1
(b) RTDNDLN_N04_T1000_P100_L28_LOFF_06072022_1

(a) (b)

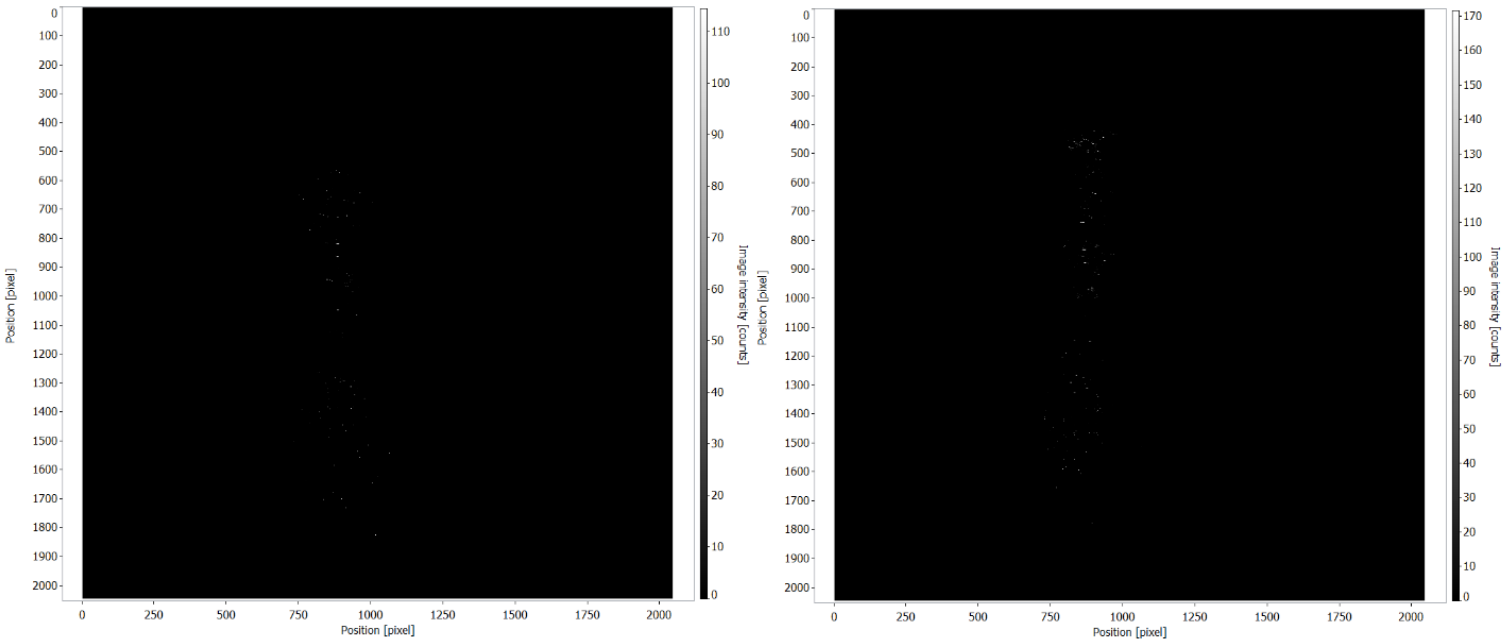

Figure 48: (a) RTDND_N04_T1000_P100_L28_LOFF_BS_06072022_1
(b) RTDNDLN_N04_T1000_P100_L28_LOFF_BS_06072022_1

(a) (b)

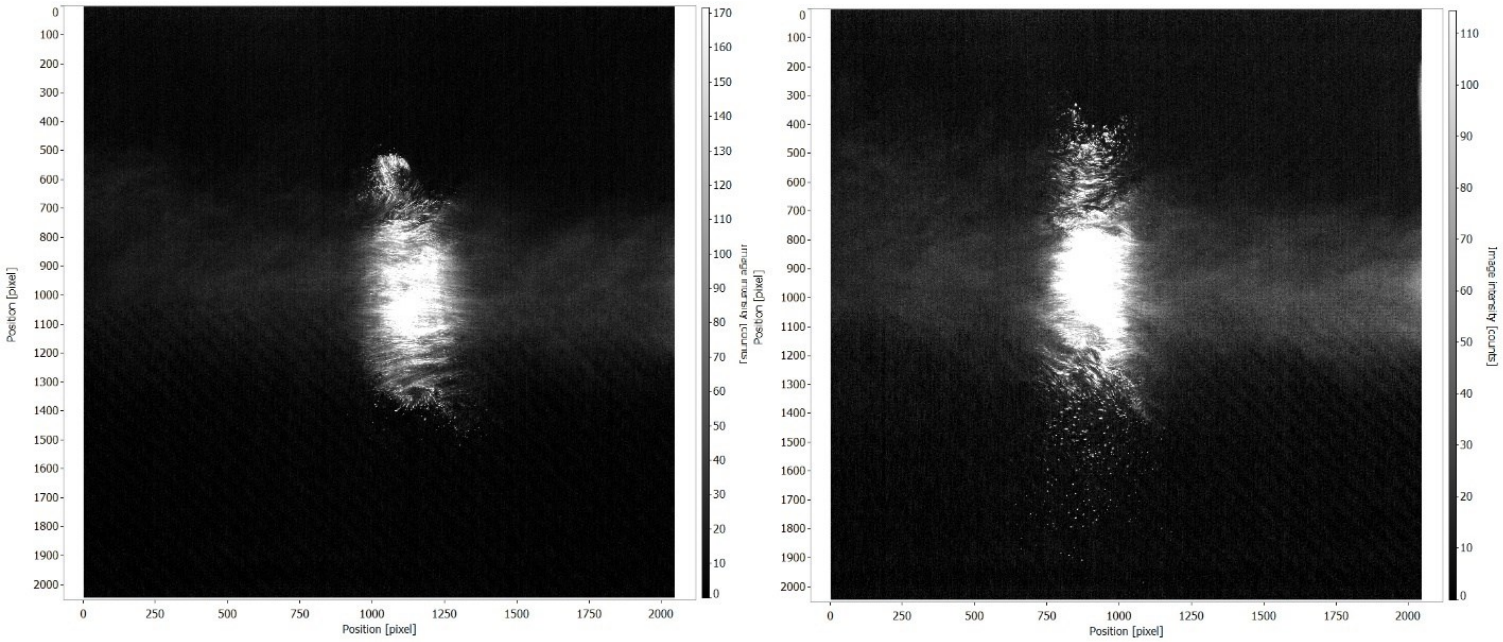

Figure 49: (a) RTDND_N04_T5000_P100_L28_LON_06072022_1
(b) RTDNDLN_N04_T5000_P100_L28_LON_06072022_1

(a) (b)

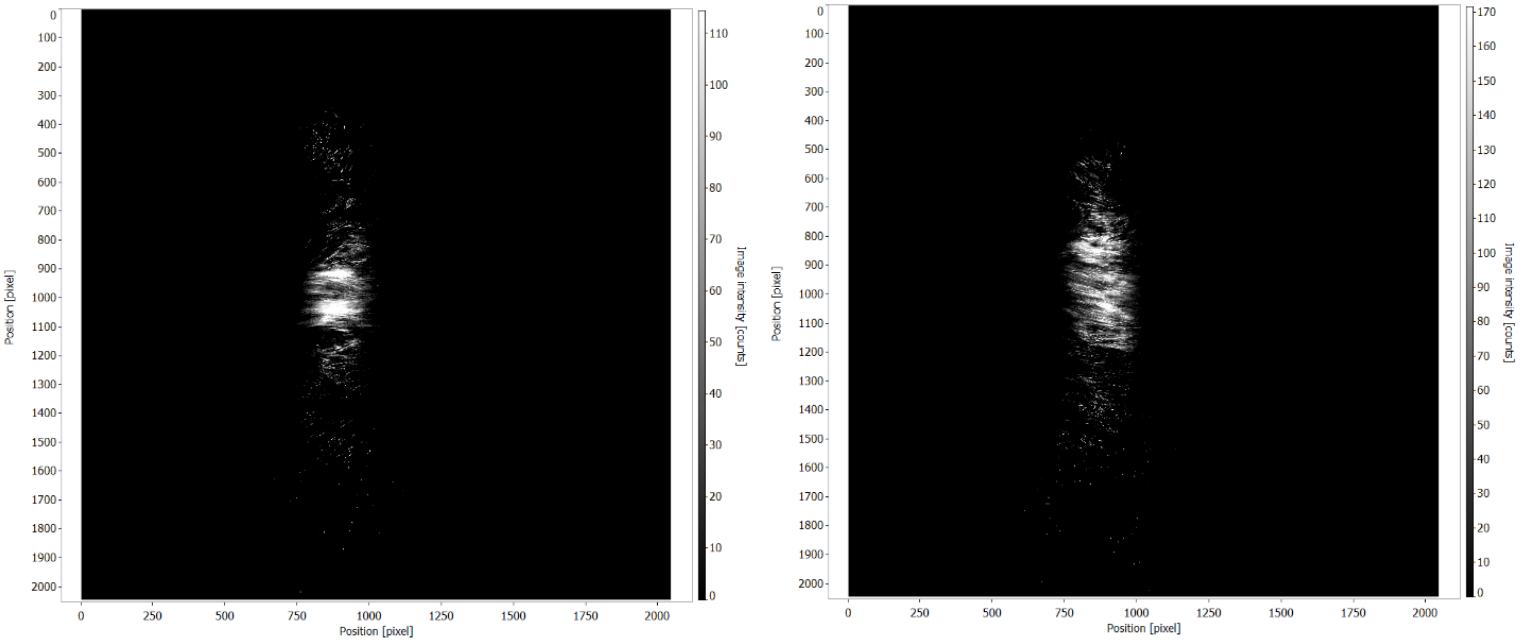

Figure 50: (a) RTDND_N04_T5000_P100_L28_LON_BS_06072022_1
(b) RTDNDLN_N04_T5000_P100_L28_LON_BS_06072022_1

(a) (b)

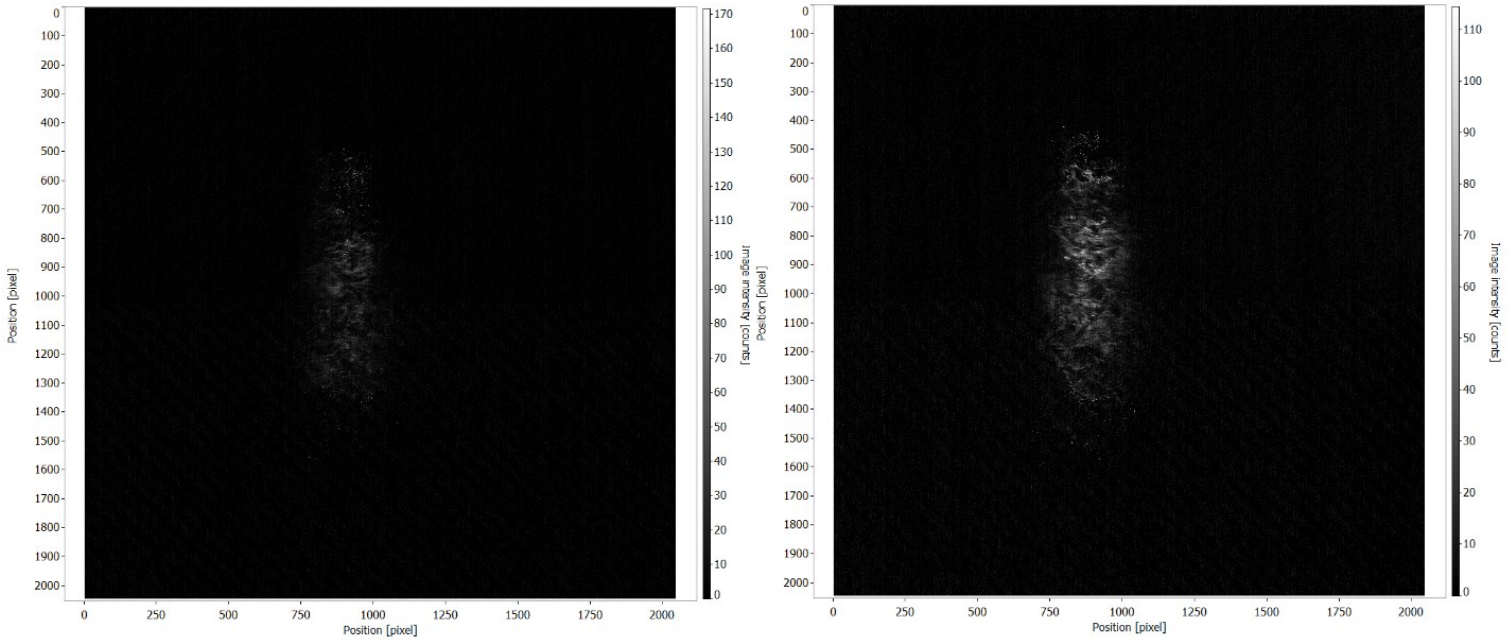

Figure 51: (a) RTDND_N04_T600_P180_L28_LOFF_06072022_1
(b) RTDNDLN_N04_T600_P180_L28_LOFF_06072022_1

(a) (b)

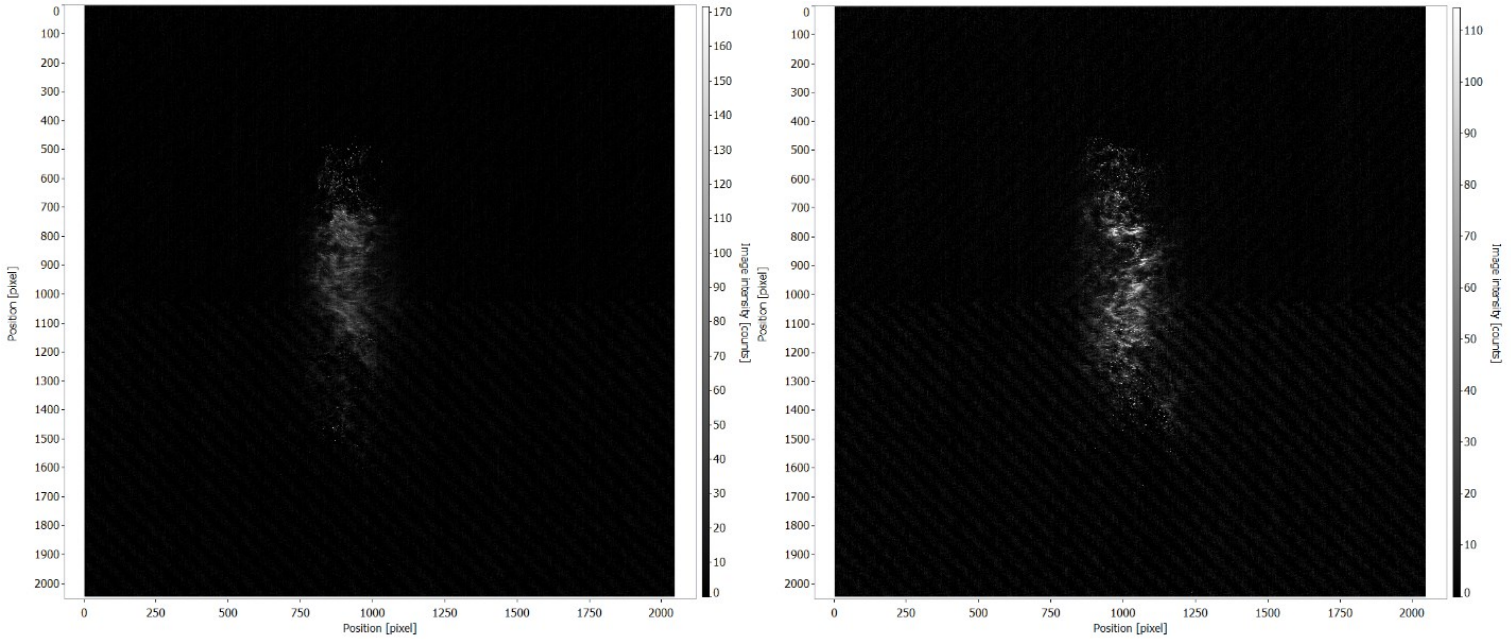

Figure 52: (a) RTDND_N04_T800_P180_L28_LOFF_06072022_1
(b) RTDNDLN_N04_T600_P180_L28_LOFF_06072022_1

(a) (b)

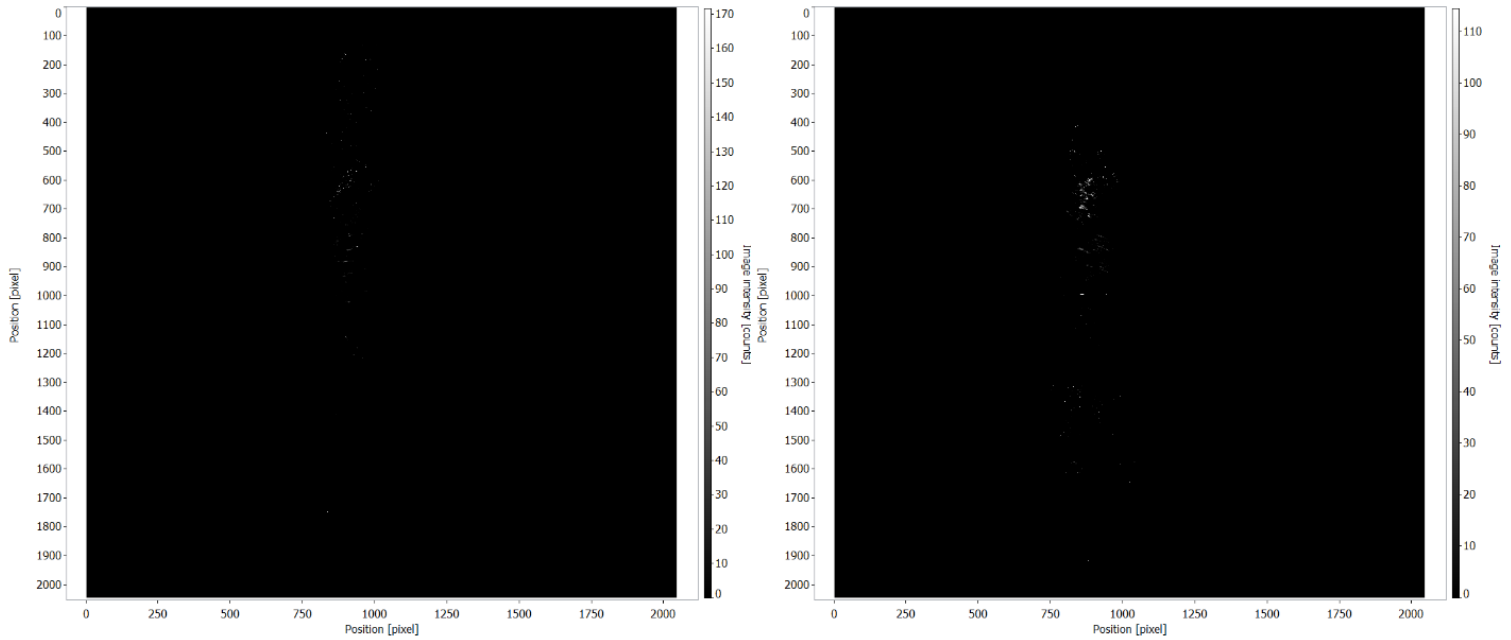

Figure 53: (a) RTDND_N04_T1000_P180_L28_LOFF_BS_06072022_1
(b) RTDNDLN_N04_T1000_P180_L28_LOFF_BS_06072022_1

(a) (b)

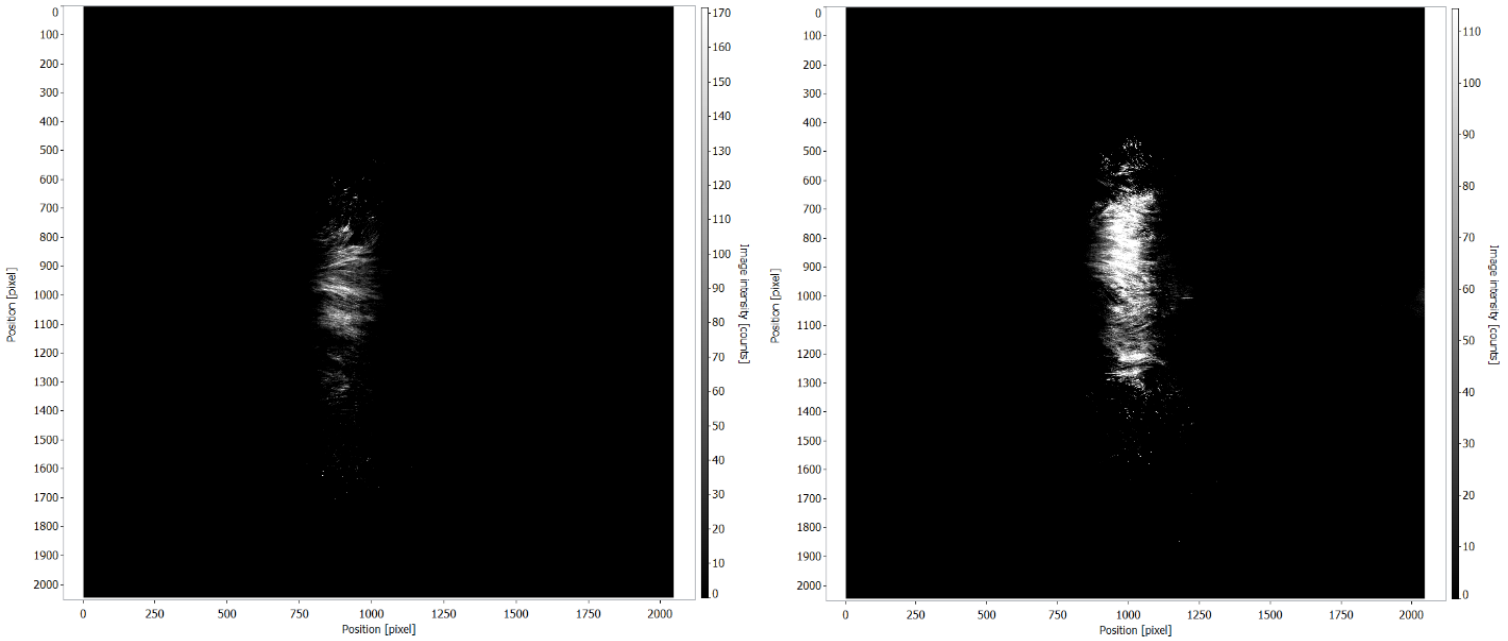

Figure 54: (a) RTDND_N04_T5000_P180_L28_LON_BS_06072022_1
(b) RTDNDLN_N04_T5000_P180_L28_LON_BS_06072022_1

(a) (b)

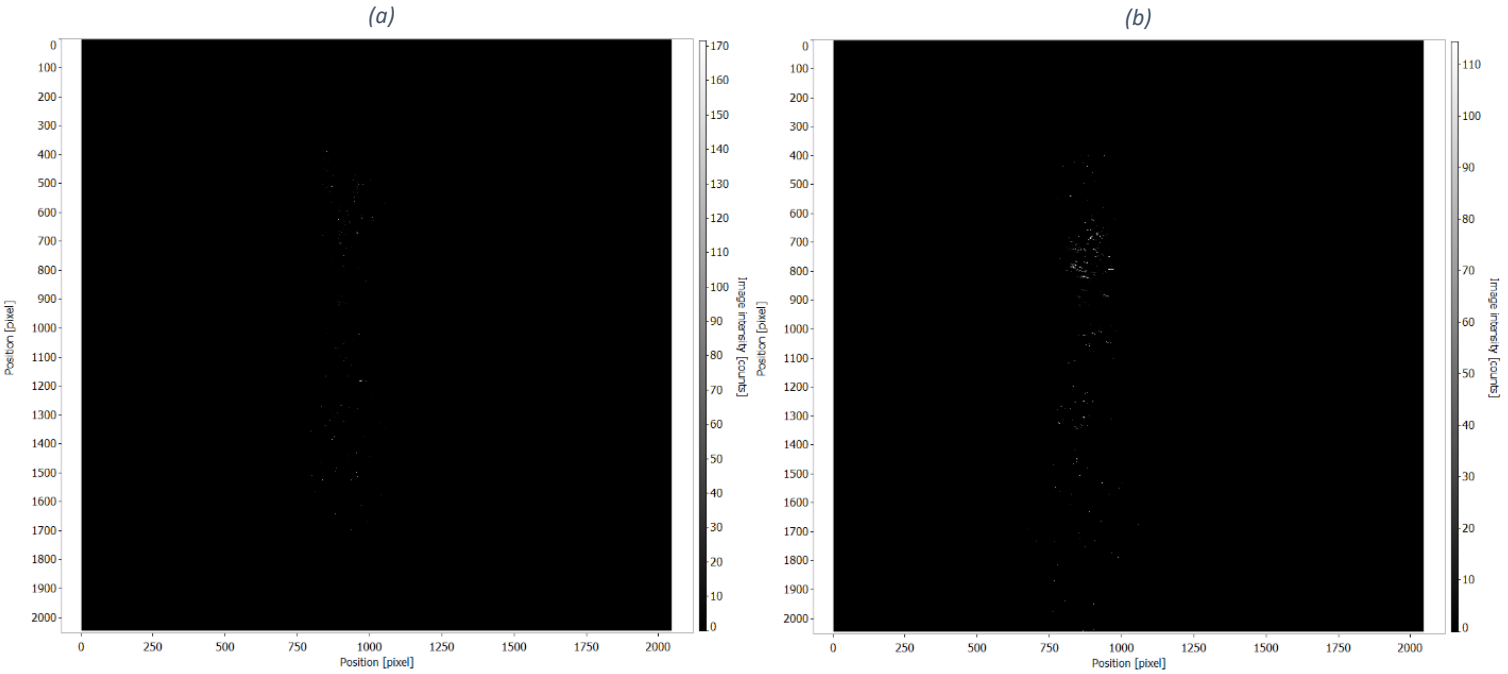

Figure 55: (a) RTDND_N04_T1000_P050_L28_LOFF_BS_06072022_1
(b) RTDNDLN_N04_T1000_P050_L28_LOFF_BS_06072022_1

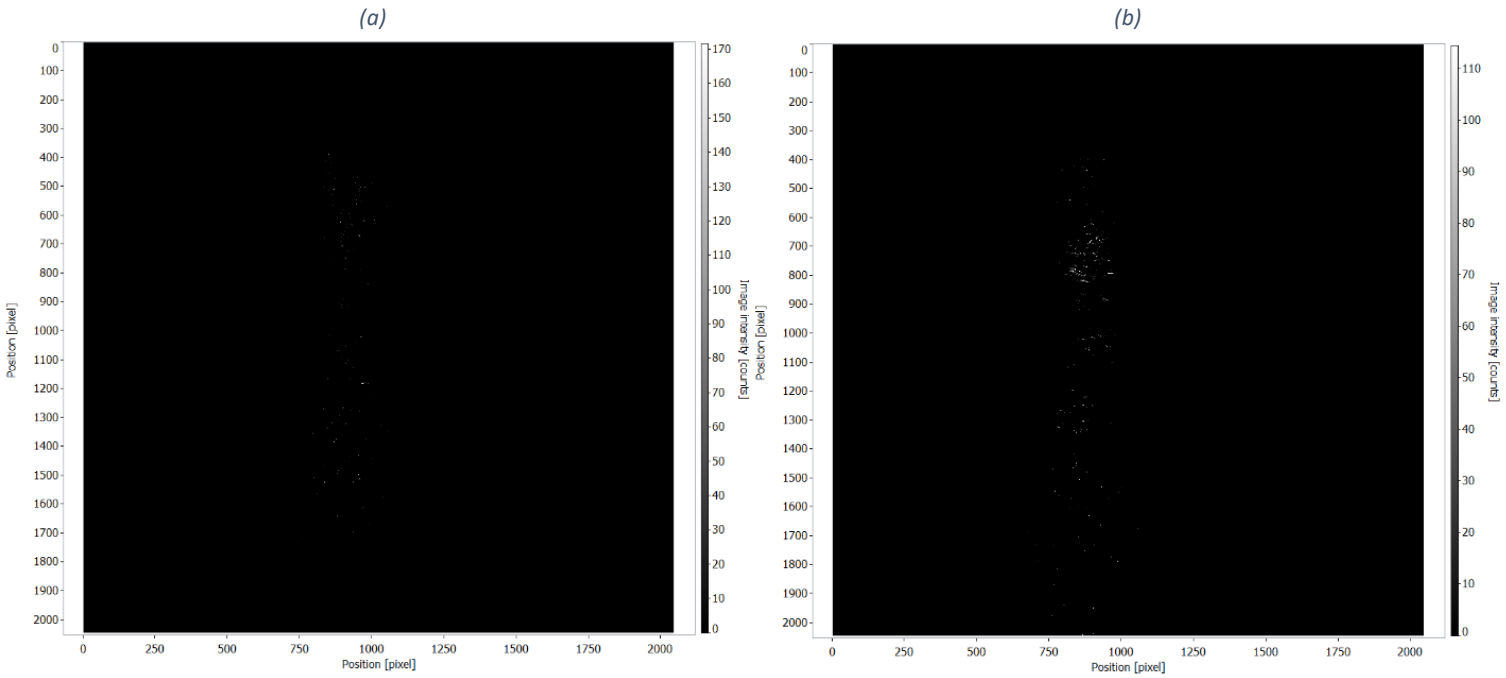

Figure 56: (a) RTDND_N04_T5000_P050_L28_LON_BS_06072022_1
(b) RTDNDLN_N04_T5000_P050_L28_LON_BS_06072022_1

During the acquisition of the NDs mixtures images some got particularly interesting when spotted. Considering the images taken with high exposure time, lower pressure and applying the background subtraction (BS), the number of single particles recognizable it's very high, with almost no path visible in the images (Figures 53, 54, 55, 56).

Due to his unexpected detailed, due to the previous behaviour of the BS on giving dark images, was taken the decision of pushing forward the study about those interesting parameter configurations, precisely the modifications are:

1. Trying with even lower pressure: 60 kPa and 30 kPa
2. Adding a middle step between 1000 ms and 5000 ms: 3000 ms
3. Trying to take the images only with the lights turned off

The image collection procedure and renaming has been kept unchanged from the previous one.

Table 6 summarize the configurations used for the NDs mixtures additional test.

Table 6: NDs sample tried parameters configuration. The green squares indicate the tried configuration

Nanodiamonds sample		Exposure time [ms]			
		800	1000	3000	5000
Aerograph configuration	N.D 0.4 mm P. 30 kPa	BS	BS	BS	BS
	N.D 0.4 mm P. 60 kPa	BS	BS	BS	BS

Legend:

N.D. = Noozle diameter **P.** = Aerograph air pressure
WaW B.S. = With and without Background Subtraction
B.S. = Only with background subtraction

Following some example images taken with different configurations for both the NDs sample mixture (RT-DND left, RT-DND-LN right) during the additional tests.

Figures from 58 to 63 show images taken with 0.4 nozzle diameter, high exposure (increasing order) time and low air pressure (60 kPa, 30 kPa).

(a) *(b)*

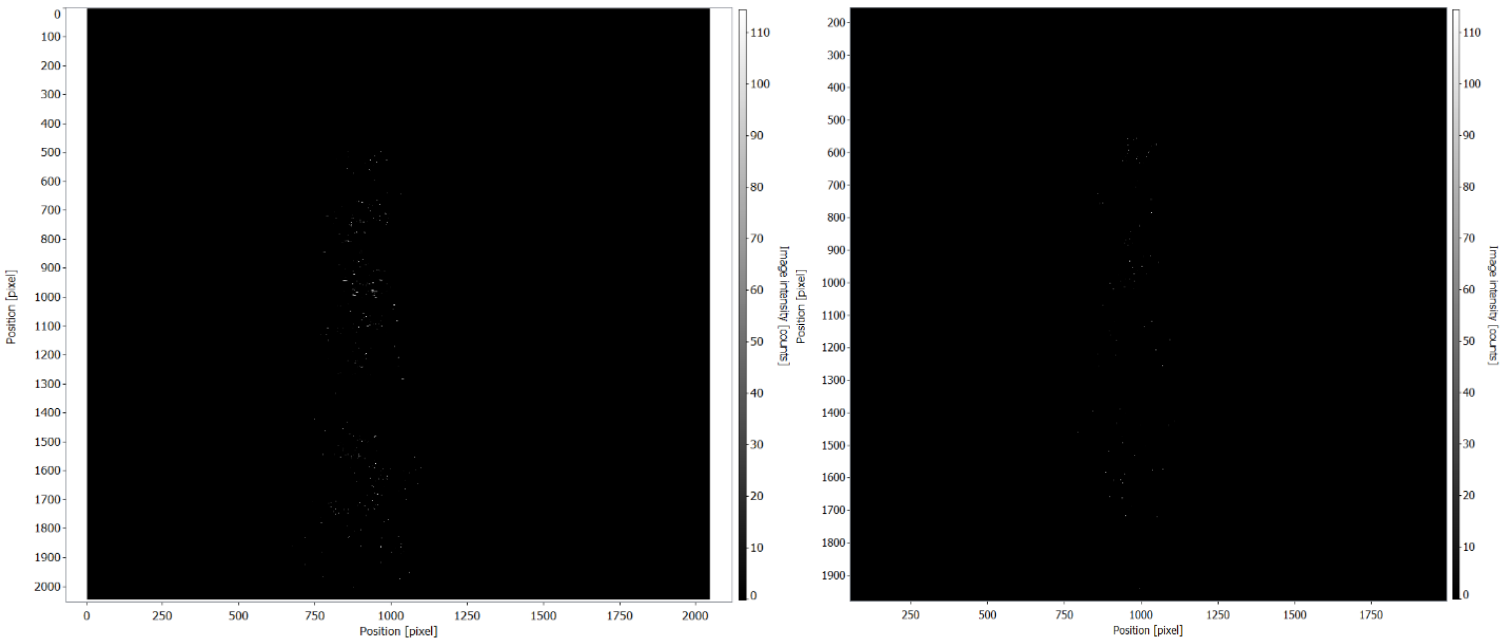

Figure 58: (a) RTDND_N04_T1000_P030_L28_LOFF_BS_07072022_1
(b) RTDNDLN_N04_T1000_P030_L28_LOFF_BS_07072022_1

(a)

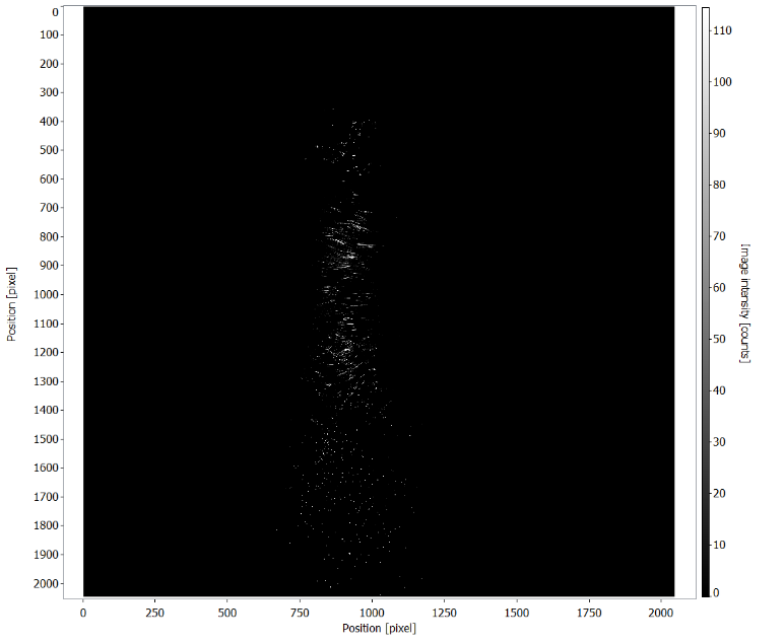

(b)

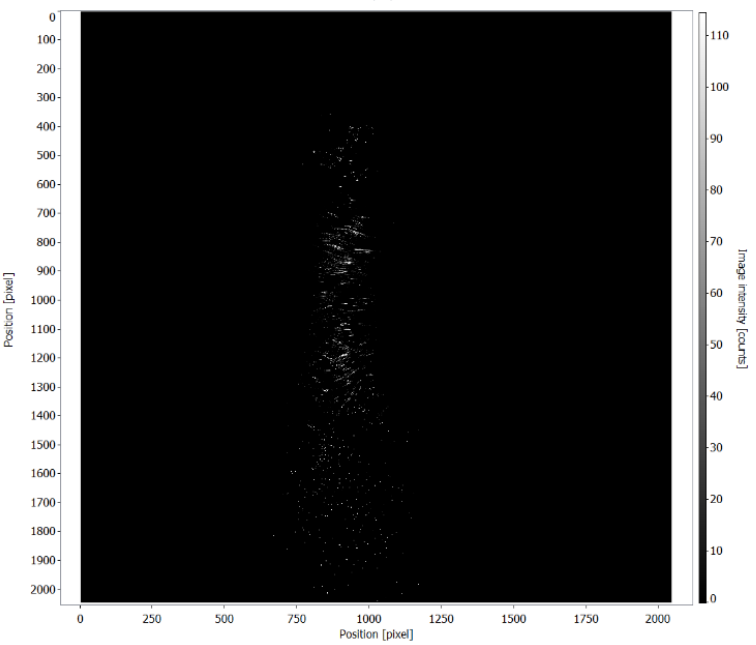

Figure 59: (a) RTDND_N04_T3000_P030_L28_LOFF_BS_07072022_1
(b) RTDNDLN_N04_T3000_P030_L28_LOFF_BS_07072022_1

(a)

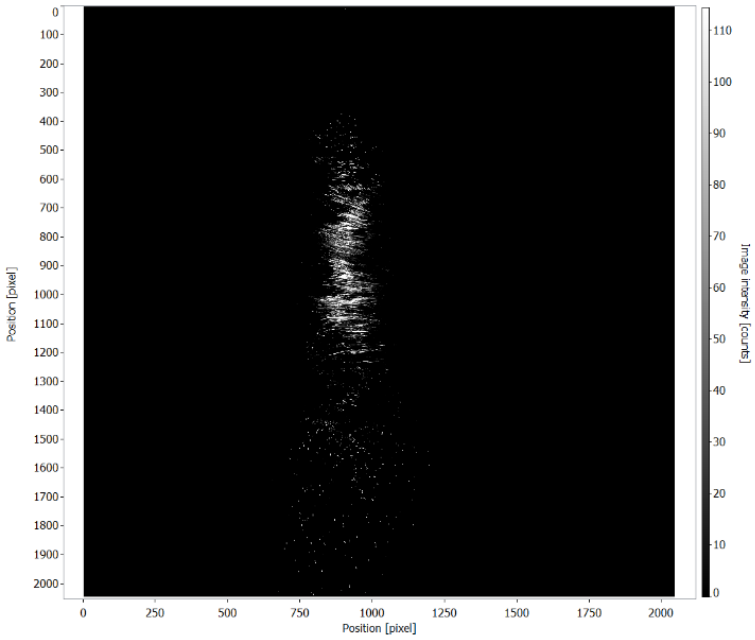

(b)

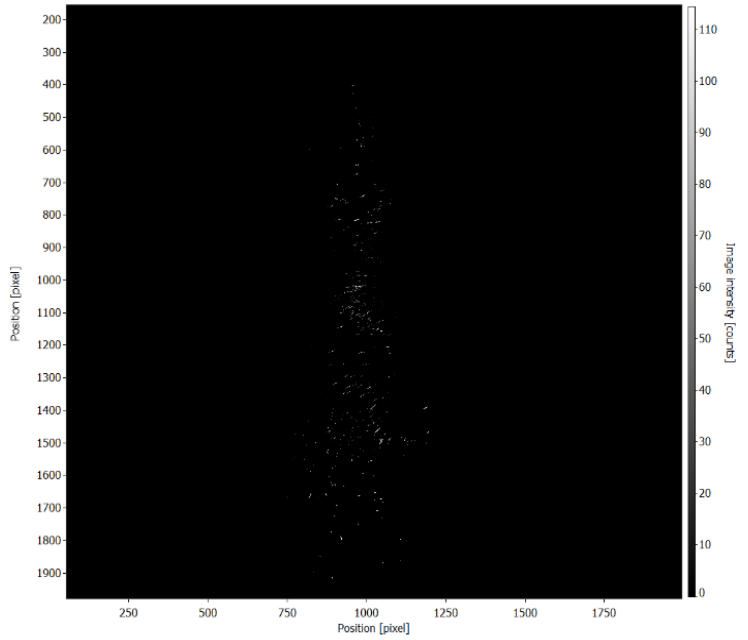

Figure 60: (a) RTDND_N04_T5000_P030_L28_LOFF_BS_07072022_1
(b) RTDNDLN_N04_T5000_P030_L28_LOFF_BS_07072022_1

(a)

(b)

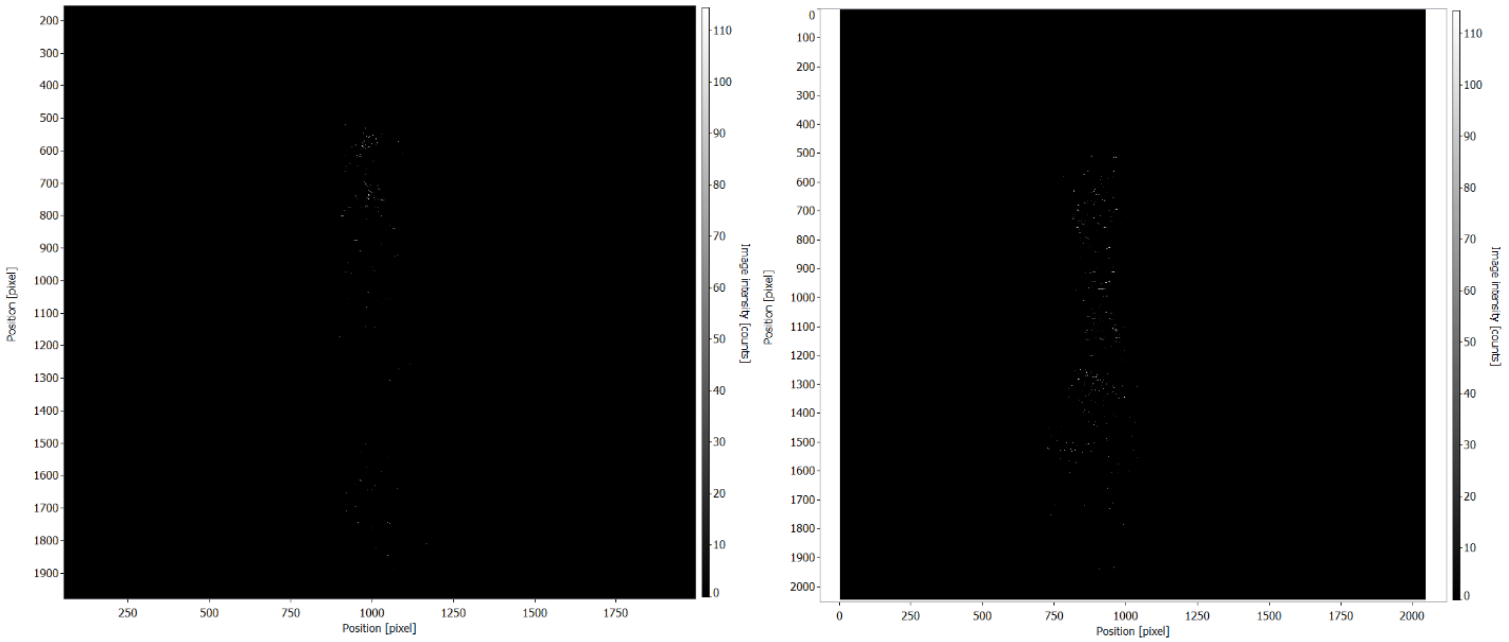

Figure 61: (a) RTDND_N04_T1000_P060_L28_LOFF_BS_07072022_1
(b) RTDNDLN_N04_T1000_P060_L28_LOFF_BS_07072022_1

(a)

(b)

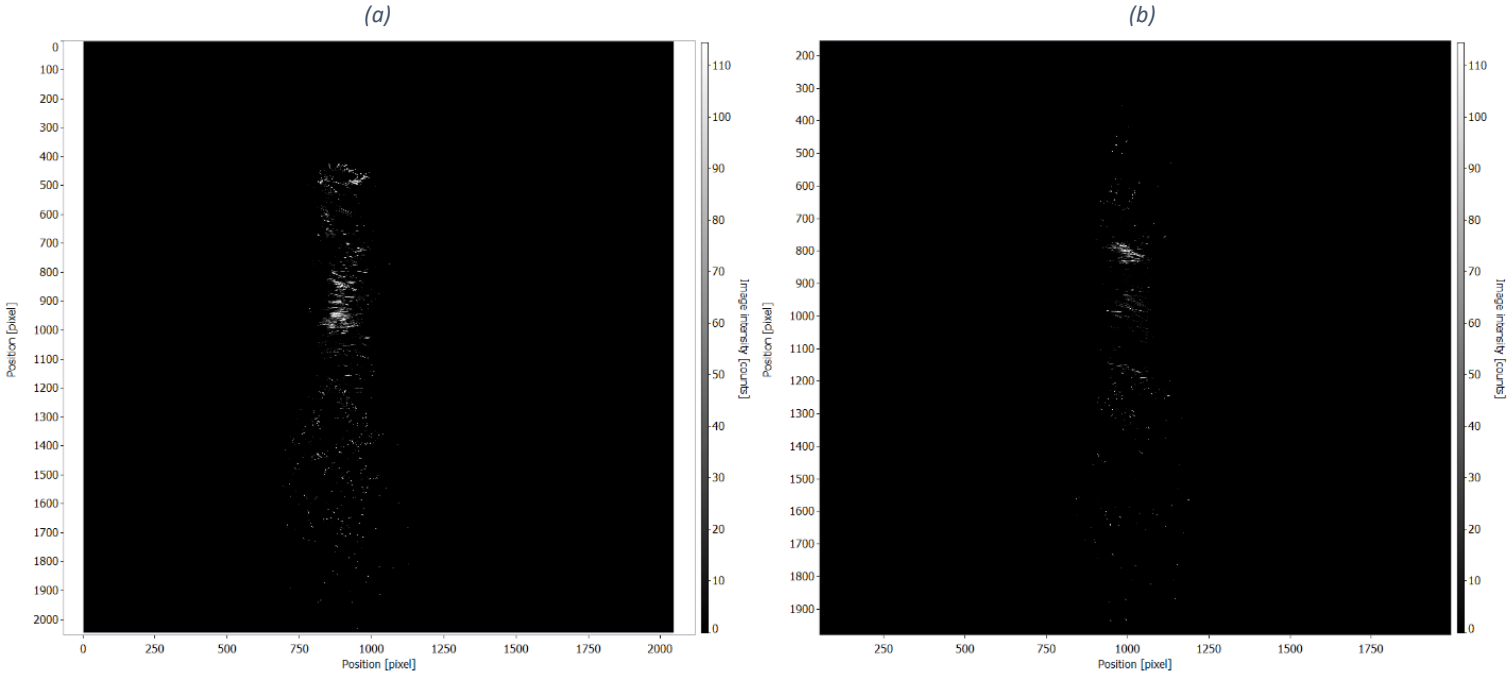

Figure 62: (a) RTDND_N04_T3000_P060_L28_LOFF_BS_07072022_1
(b) RTDNDLN_N04_T3000_P060_L28_LOFF_BS_07072022_1

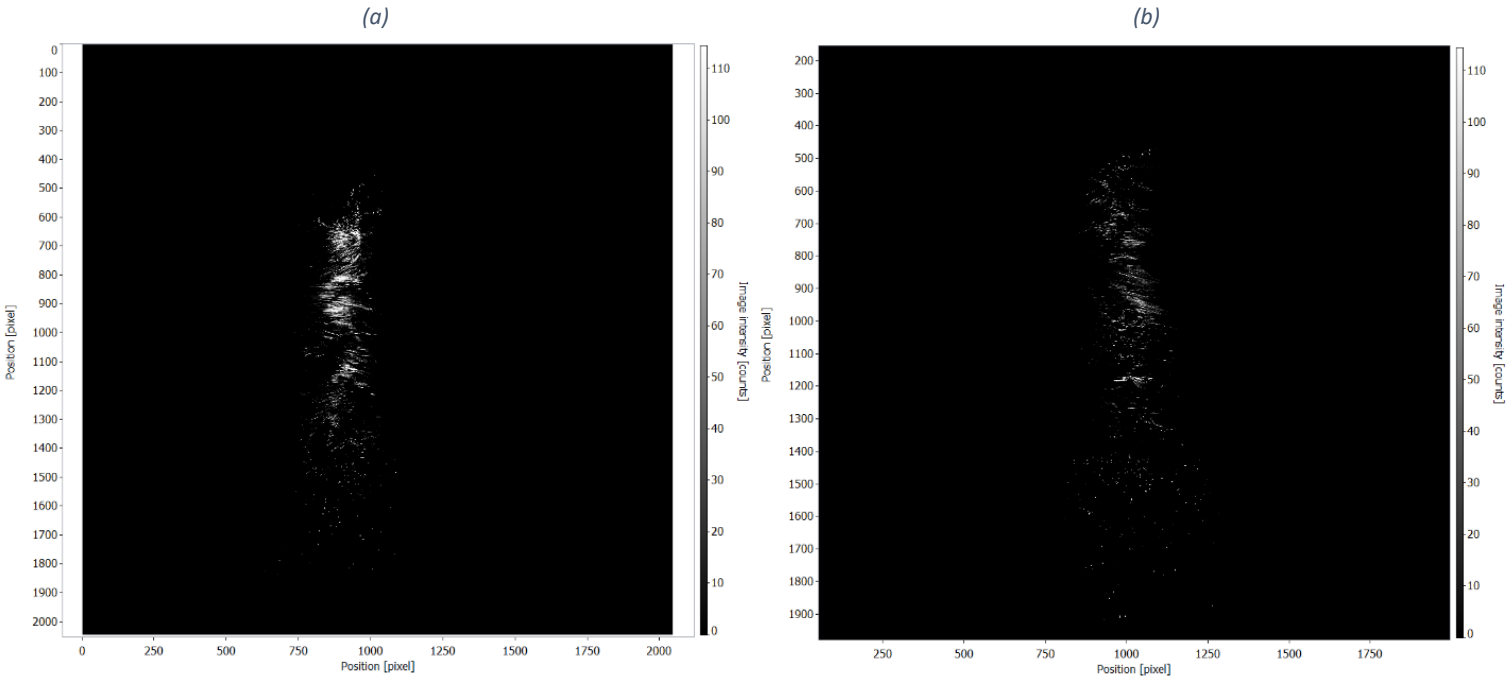

Figure 63: (a) RTDND_N04_T5000_P060_L28_LOFF_BS_07072022_1
(b) RTDNDLN_N04_T5000_P060_L28_LOFF_BS_07072022_1

5.3 Analysis of collected data

Further step to the study would have been the velocity analysis of the particles using the cross-correlation technique and statistical matters, to have some more information regarding the main paths of the stream. Due to the necessary change of equipment for the problem occurred to the laser, the camera had to be changed as well. In the used equipment the camera frequency of shutter it's lower than the original one because is used for a different kind of application (turbine air flow in wind chamber, compressors behaviour, pumps, fans working, etc.). The cross correlation needs two different images taken at a really small time difference (dt) with the purpose of recognizing the same particles pattern in a different position, but with the used camera, it's likely to believe that two consecutive images will display two different groups of particles, so speed vector study won't be possible in this experiment.

It is possible to say that the collected images are coherent with the general expectation regarding the NDs behaviour, with the interesting turn that the BS took in the middle of the experiment. The images analysis will be restricted to eye visualization and human considerations on the quality of the stream, the number of visible particles, the difference between the water and the NDs mixtures.

5.4 Results and Conclusions

Regarding the material characterization can be stated that the RT-DND-LN seem to be the best candidate for a good visualization of the NDs particles in the PIV system, thanks to the good photoluminescence properties of emitting light when excited with the proper wavelength. The Raman spectroscopy would have been helpful to this characterization but due to photobleaching phenomena of the NDs was not possible to determine any information from the test, conclusions that can be taken comparing the Raman graph from the literature and the graph made as result from the tests made with the analysed NDs samples.

Analysing the collected images, some different considerations going along with conclusions can be stated on the experiment.

The good photoluminescence properties of the NDs are well visible and some recognizable difference can be found between the demineralized water and the NDs mixtures, well visible comparing all the images taken with BS: during the water trial the BS gave dark unreadable images whereas when used for the NDs permitted the best visualization of single particles moving (Figures 59, 60, 62, 63). In general no significant difference can be recognized between the RT-DND and RT-DND-LN mixtures, probably due to the low energy of the laser, the RT-DND-LN however are clearest and brighter in numerous couple of compared images (Figures 52, 53, 54, 56, 59, etc.). It may be said that different parameters configurations can be used for different purposes: talking about the best configurations for the particles visualization (N04, T1000/3000, P030/060, L28, BS) the RT-DND seem to give a better result in visualize a big number of paths and numerous particles especially on the sides of the stream where the velocity is lower and the flow tend to form some vortexes (well visible in Figures 47, 49, 50, 52, 54) whereas the RT-DND-LN are a better candidate for single particles detection (Figures 61b, 62b, 63b). In almost all the pictures the laser plane shape can be recognized and it the brightest one even the stream flow whole shape can be found, allowing the visualization of the particles paths before and after the excitation laser plane.

The obtained results from the experiment are promising for the aim of the whole project, considering the vast range of possible application where these statements can and will be used. There is to say that some more different mixture samples can be made for verifying that the rate water/NDs is sufficient or can be raised for a better visualization of a higher number of luminescent particles.

REFERENCES

[1] S. F. Mitura, P. Niedzielski, K. Mitura, P. Louda - Nanocrystalline diamond, its synthesis, properties and applications, Journal of Achievements of Materials and Manufacturing Engineering - April 2006

[2] S. Nasir, M. Zobir Hussein, Z. Zainal, N. Azah Yusof - Carbon-Based Nanomaterials/Allotropes: A Glimpse of Their Synthesis, Properties and Some Applications, Natiomal Library of Medicine - 13 February 2018

[3] Risk Assessment of Products of Nanotechnologies, Scientific Committee on Emerging and Newly Identified Health Risks – 2009

[4] N. Baig, I. Kammakakam, W. Falath - Nanomaterials: a review of synthesis methods, properties, recent progress, and challenges, Royal society of Chemistry - 24 February 2021

[5] https://www.chimica-online.it/composti/fullerene.htm - accessed on 27 May 2022

[6] B. Yirka - Research team finds a way to accurately measure permeability of carbon nanotubes – 8 September 2016

[7] M. Mabrouk, D. B. Das, Z. A. Salem, and H. H. Beherei - Nanomaterials for Biomedical Applications: Production, Characterisations, Recent Trends and Difficulties, Journal Molecules - 18 February 2021

[8] J.C. Arnault - Nanodiamonds: Advanced Material Analysis, Properties and Applications, Chapter 2, Production, and purification of nanodiamonds, Elsevier Inc - 2017

[9] Applications of diamond grits and composites. In: The Properties of Natural and Synthetic Diamond (ed. J.E. Field), 669 – 1992 - Academic Press.

[10] H.C. Chang, W. Wei-Wen Hsiao, M.C. Su - Fluorescent Nanodiamonds, Chaptre 3, Color centers in nanodiamonds, John Wiley & Sons Ltd . 2019

[11] R.W. Powl - Electron conductivity and photochemical processes in alkali‐halide crystals. Proc Phys Soc (London) 49 (supplement): 3‐31. - 1937

[12] R. F. Mould - Sir William Crookes (1832–1919) Biography with special reference to X-rays - 2017

[13] J.X. Qin, X.G. Yang, C.F.Lv, Y.Z. Li, K.K. Liu, J.H. Zang, X. Yang, L. Dong, C.X. Shan - Nanodiamonds: Synthesis, properties, and applications in nanomedicine - 6 September 2021

[14] E. J. Stamhuis - Basics and principles of particle image velocimetry (PIV) for mapping biogenic and biologically relevant flows - 26 April 2005

[15] M.D. Atkins - in Application of Thermo-Fluidic Measurement Techniques, Velocity Field Measurement Using Particle Image Velocimetry (PIV) – 2016

[16] Willert and Gharib 1901 - Stamhuis and Videler 1995 - Adrian 1991

[17] Z. Daniel, D. R. Mueller, M. C. Richmond - Study of Fish Response Using Particle Image Velocimetry and High-Speed - October 2004

[18] B. Wieneke - PIV Uncertainty Quantification and Beyond - December 2017

[19] OpenPIV group Revision fa029e16 - Basics of Particle Image Velocimetry (PIV) 2014

[20] A.M. Vervald, S.A. Burikov, A.M. Scherbakov, O.S. Kudryavtsev, N.A. Kalyagina, I.I. Vlasov, E.A. Ekimov, T.A. Dolenko - Boron-doped nanodiamonds as anticancer agents: En route to hyperthermia/thermoablation therapy, ACS Biomater - Sci. Eng. 6 (8) (2020) 4446–4453.

[21] X.-Q. Zhang, R. Lam, X. Xu, E.K. Chow, H.-J. Kim, D. Ho - Multimodal nanodiamond drug delivery carriers for selective targeting, imaging, and enhanced chemotherapeutic efficacy - Adv. Mater. 23 (41) (2011) 4770– 4775.

[22] U. Roy, V. Drozd, A. Durygin, J. Rodriguez, P. Barber, V. Atluri, X. Liu, T.G. Voss, S. Saxena, M. Nair - Characterization of nanodiamond-based anti-HIV drug delivery to the brain - Sci. Rep. 8 (2018) 1603.

[23] Ray Techniques LTD. Nanodiamond Technologies online products catalogue - https://www.nanodiamond.co.il/Powders - - accessed on 9 June 2022

[24] OMNI International main site for reference - OMNi-inc.com//omni-sonic-ruptor-400-ultrasonic-homogenizer.html – 2021- accessed on 10 June 2022

[25] C.V. Raman & K. S. Krishnan - A New Type of Secondary Radiation, Nature 121, 501- 502 - 1928

[26] Smith & G. Dent - Modern Raman Spectroscopy: A Practical Approach 1st ed. , Wiley – 2005

[27] V. Y. Osipov, S. A. Zargaleh, F. Treussart, F. M. Shakhov - Photoluminescence from NV − Centres in 5 nm Detonation Nanodiamonds: Identification and High Sensitivity to Magnetic Field in Nanoscale Research Letters - August 2019

[28] O. Faklaris, D. Garrot, P. Curmi, P. Curmi - Comparison of the photoluminescence properties of semiconductor quantum dots and non-blinking diamond nanoparticles. Observation of the diffusion of diamond in Journal of the European Optical Society Rapid Publications - May 2009

[29] Horiba Scientific on-line products cathalog - https://www.horiba.com/pol/scientific/- accessed on 5 Jul 2022

[30] Edinburg Instruments products cathalog - https://www.edinst.com/us/products/fls-980-fluorescence-spectrometer/- accessed on 5 Jul 2022

[31] LaVision on-line products cathalog, section Cameras for PIV - https://www.lavision.de/en/products/cameras/cameras-for-piv/ - accessed on 5 Jul 2022

[32] Laser point Factory on-line products cathalog - https://www.laserpointerfactory.com/product/l303-red-and-green-two-different-color-laser-pointer-light-2/ - accessed on 5 Jul 2022

[33] LaVision on-line products cathalog, section Calibration Plates - https://www.smart-piv.com/en/products/strainmaster/system-components/calibration-plates/ - accessed on 5 Jul 2022

[34] Harder & Steenback on-line products cathalog - https://www.harder-airbrush.eu/en/more.html - accessed on 5 Jul 2022

[35] LaVision on-line products cathalog, section software - https://www.lavision.de/en/products/davis-software/- accessed on 5 Jul 2022

[36] V. Vaijayanthimala, H-C Chang - Functionalized fluorescent nanodiamonds for biomedical applications - 19 Dec 2008- accessed on 5 Jul 2022

[37] V. I. Korepanov, H. Hamaguchi, E. Osawa, V. Ermolenkov, I. K. Lednev, B. J. M. Etzold, O. Levinson, B Zousman, C. Prakash Epperla, H. C. Chang - Carbon structure in nanodiamonds elucidated from Raman spectroscopy - 3 June 2017

[38] Z. Novak, A. Karczemska, D. Witkowski – Analysis of the Nanodiamonds Emission used in Absorbable Collagen Dressing in Preparation for Particle Image Velocimetry System. - 2022